Industrial Chemistry & Materials

Accepted Manuscript

This article can be cited before page numbers have been issued, to do this please use: J. Park, J. Cherusseri, J. Theerthagiri, A. Min, A. Kumar, G. Kim, N. R. Bharadwaj, S. Lee, R. I. R.S. and M. Y. Choi, *Ind. Chem. Mater.*, 2026, DOI: 10.1039/D6IM00053C.

View Article Online
DOI: 10.1039/D6IM00053C

Levitation-guided disorder engineering unlocks efficient nitrite-to-ammonia electroconversion

Juhyeon Park,[†a] Jayesh Cherusseri,[†a] Jayaraman Theerthagiri,[†a] Ahreum Min[†a] Anuj Kumar,[†b] Gyeong-Ah Kim,[c] Nivarthi Rajiv Bharadwaj,[a] Sanggyeong Lee,[a] Rimal Isaac R.S[d] and Myong Yong Choi*[ac]

[a] Department of Chemistry (BK21 FOUR), Research Institute of Advanced Chemistry, Gyeongsang National University, Jinju 52828, Republic of Korea

[b] Nano-Technology Research Laboratory, Department of Chemistry, GLA University, Mathura, Uttar Pradesh 281406, India

[c] Core-Facility Center for Photochemistry & Nanomaterials, Gyeongsang National University, Jinju 52828, Republic of Korea

[d] Department of Nanotechnology, Noorul Islam Centre for Higher Education, Kumaracoil, Thuckalay, Kanyakumari, Tamil Nadu 629180, India

* Corresponding author E-mail: mychoi@gnu.ac.kr (M. Y. Choi)

† These authors contributed equally to this work

View Article Online
DOI: 10.1039/D6IM00053C

Electrocatalytic conversion of nitrite (NO_2^-) to ammonia (NH_3) via the NO_2^- reduction reaction (eNO_2RR) presents a promising approach. Prussian Blue analogs (PBAs)–based electrocatalysts are potential candidates for eNO_2RR owing to their good activity and selectivity. Herein, to the best of our knowledge, for the first time, we report a facile synthesis of a flower-like copper–cobalt PBA sulfide (CuCoPBA-S) using pulsed laser irradiation in liquid and investigate its formation mechanism using acoustic levitation coupled with *in situ* Raman spectroscopy. This approach enables contaminant-free, rapid, and cost-effective synthesis of electrocatalysts. The sulfidation process is shown to be time-dependent in the formation of ordered/disordered flower-like CuCoPBA-S structures. The CuCoPBA-S considerably influences the eNO_2RR, achieving a Faradaic efficiency (FE) of 80.91% and an NH_3 yield rate (YR (NH_3)) of 3394.1 μg h^{-1} cm^{-2} at a fixed potential of −0.5 V vs. the reversible hydrogen electrode (RHE). Moreover, density functional theory analysis validates the eNO_2RR pathway facilitated by CuCoPBA-S during the electrocatalytic conversion of NO_2^- to NH_3, and the rate-determining step in the pathway is the hydrogenation of $*NH_2O$ to $*NH_2OH$.

Keywords: Prussian blue analog; Acoustic levitation; Nitrite reduction; Electrocatalysis; Ammonia synthesis.

1 Introduction

Nitrate and nitrite (NO_2^-), are the water contaminants, pose a serious threat to daily life owing to its adverse effect of blocking the oxygen transport in blood vessels. [1, 2] Hence, its removal from water bodies is essential, though the process typically demands substantial energy. A

View Article Online
DOI: 10.1039/D6IM00053C

sustainable approach that removes nitrate/NO_2^- through a catalytic process while simultaneously generating energy offers a versatile solution aligned with *Sustainable Development Goal 6: Clean Water and Sanitation* and *Sustainable Development Goal 7: Affordable and Clean Energy*, as set by the United Nations. The ultimate objective of wastewater treatment is the complete reduction of nitrate/NO_2^- to value-added products such as nitrogen (N_2) or ammonia (NH_3). Photocatalytic and electrocatalytic approaches have been widely explored for nitrate and NO_2^- reduction. Among these, conversion of nitrate to NH_3 via electrocatalytic nitrate reduction reaction and NO_2^- to NH_3 via electrocatalytic NO_2^- reduction reaction (eNO_2RR) has become a viable option for electrochemists, enabling the production of NH_3 under ambient conditions. [3, 4] Although nitrate is more abundant in natural and industrial environments, NO_2^- plays a critical role as a key intermediate in the nitrate reduction pathway and is frequently present in wastewater streams originating from agricultural runoff, biological nitrification–denitrification processes, and industrial effluents. Under incomplete denitrification conditions, NO_2^- can accumulate and persist at appreciable concentrations, making its selective removal both environmentally important and necessary to prevent secondary pollution.

NH_3 is an essential feedstock for the manufacture of fertilizers, pharmaceuticals, and other industrial chemicals. [5-7] Currently, large-scale NH_3 production relies predominantly on the Haber–Bosch process, which is associated with high energy consumption. [8] Although the catalytic nitrogen reduction reaction provides an alternative route to NH_3 synthesis, it is limited by the low solubility of N_2 in aqueous electrolytes and the high dissociation energy of the N≡N bond (~ 914 kJ mol^{-1}). In contrast, electrocatalytic nitrate reduction reaction and eNO_2RR offer more feasible pathways for NH_3 production. Notably, NO_2^- is a more readily reducible nitrogen source than dinitrogen, enabling lower overpotentials and higher reaction efficiencies. Our focus

View Article Online
DOI: 10.1039/D6IM00053C

on NO_2^- reduction is motivated by both mechanistic and practical considerations. From a fundamental perspective, eNO_2RR involves fewer proton-coupled electron transfer steps than nitrate reduction, enabling clearer identification of intrinsic catalytic activity and reaction pathways. This makes NO_2^- an ideal model substrate for probing catalytic active sites and reaction kinetics, which can inform the rational design of catalysts for the more complex nitrate reduction process. From an application standpoint, although large-scale NH_3 production directly from NO_2^- may be limited by feedstock availability, NO_2^--containing streams are commonly encountered in decentralized and intermediate stages of nitrogen treatment systems, where localized NH_3 production could be feasible. Furthermore, mechanistic insights gained from eNO_2RR are directly transferable to nitrate reduction systems, as NO_2^- is an essential intermediate in the overall nitrate-to-NH_3 conversion pathway. Thus, eNO_2RR provides a dual benefit: effective removal of toxic nitrogen-containing contaminants from water and simultaneous NH_3 generation, making it a key focus in sustainability research. In this context, eNO_2RR presents a feasible and low-cost process for NH_3 production. [9] This approach integrates wastewater remediation with value-added chemical production and supports the development of a circular nitrogen economy. Despite these advantages, eNO_2RR still faces limitations, including low yield, limited selectivity, and the high cost of catalysts. [10] Therefore, the rational design of efficient and economical electrocatalysts is critical for improving eNO_2RR performance. [11]

Consequently, nanostructured catalysts with high electrical conductivity, catalytic activity, stability, and selectivity are essential prerequisites for efficient eNO_2RR. [12] Noble metal catalysts, such as platinum (Pt), [13] gold (Au), [14] silver (Ag), [15] ruthenium (Ru), [16] palladium (Pd), [1] and iridium (Ir) [17] are suitable candidates with high eNO_2RR selectivity and NH_3 product yield. However, owing to the high cost of noble metals, developing low-cost catalysts for the eNO_2RR

View Article Online
DOI: 10.1039/D6IM00053C

process is imperative. Tremendous efforts have been involved for developing non-noble metal catalysts, such as copper (Cu), cobalt (Co), nickel (Ni), and iron (Fe). Among these, Cu and Co have received much attention owing to their excellent selectivity toward eNO_2RR, strong activity, and high Faradaic efficiency (FE). The hydrogen evolution reaction (HER) is a competing process that adversely affects the eNO_2RR activity of the electrocatalyst. Cu/Co-based electrocatalysts exhibit low or negligible HER activity and are therefore highly favored for eNO_2RR. [18] Natural abundance, high NO_2^- selectivity, and fast reaction kinetics further enhance the appeal of Cu/Co-based catalysts. [19] In this context, the synthesis of Cu/Co-based electrocatalysts with nanostructured morphologies offers a cost-effective and viable approach for synthesizing catalysts. Recent studies highlight the effectiveness of nanostructured Cu/Co-based catalysts. For example, isolated Cu atoms anchored on MnO_2 achieved an NH_3 yield rate (YR (NH_3)) of 439.8 μmol h^{-1} cm^{-2} with a FE (NH_3) of 93.3%. [20] Wang et al. reported an indium (In)-Cu single-atom alloy (In_1Cu) catalyst that delivered an YR (NH_3) of 1042.1 μmol h^{-1} cm^{-2} and a FE (NH_3) of 94.7% at 354 mA cm^{-2}. [21] Cobalt metallopeptide catalysts have also demonstrated eNO_2RR performance in aqueous buffers near neutral pH, achieving an FE (NH_3) of 90 ± 3% [18], while cobalt sulfide (CoS_2) nanorods supported on nickel foam reached an FE (NH_3) of 97.9% and selectivity of 98.7%. [22] A Pd/CuO electrocatalyst in 0.1 M K_2SO_4 containing 0.01 M KNO_2 achieved an YR (NH_3) of 906.4 μg h^{-1} cm^{-2} at −0.84 V vs. RHE. [23] Co@JDC composite in 0.1 M NaOH with 0.1 M NO_2^- electrolyte delivered a high YR (NH_3) of 2.8 ± 0.1 mol h^{-1} g^{-1} at −1.0 vs. RHE. [24] $Cu@TiO_2$/TP in 0.1 M Na_2SO_4 containing 0.1 M NO_2^- achieved a YR (NH_3) of 760.5 μmol h^{-1} cm^{-2} at −0.8 V vs. RHE. [25] Other representative catalysts include Cu_3P in 0.1 M PBS with 0.1 M $NaNO_2$, which delivered an YR (NH_3) of 1626.6 ± 36.1 μg h^{-1} cm^{-2} at −0.5 V vs. RHE [26], and CoB in 0.1 M Na_2SO_4 with 400 ppm NO_2^-, which achieved a YR (NH_3) of 233.1

View Article Online
DOI: 10.1039/D6IM00053C

μmol h^{-1} cm^{-2} at −0.7 V vs. RHE. [27] Additionally, a CoP electrocatalyst demonstrated a YR (NH_3) of 2260.7 ± 51.5 μg h^{-1} cm^{-2} at −0.2 V vs. RHE in 0.1 M PBS containing 500 ppm NO_2^- electrolyte.[28]

Prussian Blue and Prussian Blue analogs (PBAs), members of the metal–organic framework family, have received great attention in electrocatalysis owing to their peculiar characteristics such as good electronic conductivity, excellent electrocatalytic activity, strong electrochemical stability, and low cost. [29, 30] The structural tunability of PBAs is a fascinating feature that enables their application in eNO_2RR. For instance, PBA-derived high-entropy oxides have been reported as efficient eNO_2RR electrocatalysts, achieving a YR (NH_3) of 894.3 μg h^{-1} cm^{-2} and a FE (NH_3) of 88.9% at −1.0 V vs. Ag/AgCl. [31] While Cu/Co-based catalysts have been extensively studied for NO_3RR, their application in eNO_2RR remains comparatively underexplored. Xin et al. demonstrated a bimetallic Cu@Co-MOF-74 catalyst for NO_3RR with a YR (NH_3) of 307.98 mmol h^{-1} g_{cat}^{-1} and a FE (NH_3) of 84.01% at −0.88 V vs. RHE. [32] He et al. reported a Cu−Co binary sulfide catalyst enabling high-rate tandem electroreduction to NH_3, achieving a YR (NH_3) 1.17 mmol cm^{-2} h^{-1} in 0.1 M NO_3^- at −0.175 V vs. RHE. [33] Similarly, a $CoCuO_x$@CuO_x/Cu foam catalyst delivered an YR (NH_3) of 519.1 μg h^{-1} cm^{-2} with an FE (NH_3) of 99.83% in 1 mM NO_3^- electrolyte at −0.2 V vs. RHE. [34]

The synthesis methods of catalysts for the electroconversion of NO_2^- to NH_3 include high-temperature pyrolysis, [35] hydrothermal/solvothermal method, [36, 37] and pulsed laser deposition. [38] Pulsed laser irradiation in liquid (PLIL) has emerged as a green route for synthesizing catalyst materials in a short processing time in an environmentally friendly manner. [39-41] PLIL is a simple process for producing high-yield materials. [42, 43] Electrocatalysts prepared via PLIL have shown remarkable versatility and efficiency for converting nitrogen-containing

View Article Online
DOI: 10.1039/D6IM00053C

compounds to NH_3. Acoustic levitation coupled with PLIL is a versatile method that enables free-standing material synthesis through the formation of single droplets. [44, 45] A key advantage of this method is the elimination of the possible interactions of chemical agents with solid surfaces or boundary effects. [46, 47] Electrocatalysts can easily be synthesized in an ultraclean and confined environment that allows *in situ* analysis using characterization tools such as ultraviolet–visible (UV–Vis) or Raman spectroscopy. [48] The simultaneous synthesis and characterization is time saving and have attracted considerable research interest, especially in electrocatalysis.

The electrocatalytic conversion of NO_3^- to NH_3 proceeds through an eight-electron transfer pathway, whereas eNO_2RR involves a six-electron transfer process and remains comparatively less explored than NO_3RR. [49] This knowledge gap has motivated us to investigate the catalytic activity and reaction mechanisms of eNO_2RR using hierarchical $Cu_3[Co(CN)_6]_2$ (denoted as CuCoPBA) cubes and flower-like CuCoPBA sulfide (CuCoPBA-S) catalysts. Herein, we report the synthesis of CuCoPBA-S via a two-step process involving co-precipitation, followed by PLIL acoustic levitation coupled with PLIL. During the formation of CuCoPBA-S, a time-dependent sulfidation was observed and its mechanism was studied. CuCoPBA cubes transformed into a flower-like ordered/disordered CuCoPBA-S heterostructure during sulfidation. The sulfidation mechanism in CuCoPBA was investigated through *in situ* Raman spectroscopy. Furthermore, the electrocatalytic performance of CuCoPBA-S toward eNO_2RR was evaluated in alkaline electrolyte (1.0 M KOH) both in the absence and presence of 0.1 M KNO_2. The alkaline medium was selected because it enhances reaction kinetics, stabilizes key nitrogen-containing intermediates, suppresses competing side reactions such as HER, and provides high ionic conductivity. The YR (NH_3) during the eNO_2RR was quantified using UV–Vis spectroscopy using the Indophenol Blue method and validated via $^{14}NH_4^+$ isotope–labeling study. Density functional theory (DFT) analysis was used

View Article Online
DOI: 10.1039/D6IM00053C

to evaluate the effect of structural-oriented active sites in ordered/disordered CuCoPBA-S on the eNO_2RR activity. This study highlights the novel use of acoustic levitation coupled with PLIL to elucidate the formation mechanism of the ordered/disordered CuCoPBA-S heterostructure using *in situ* Raman spectroscopy.

2 Results and discussion

2.1 Microstructure and surface morphology

The coprecipitation method is a versatile method for synthesizing metal nanostructures with desired morphologies and sizes. We synthesized CuCoPBA using a facile coprecipitation method, which was further converted to CuCoPBA-S through photoreduction via the PLIL method. Fig. 1a shows a schematic of the synthesis of CuCoPBA-S using CuCoPBA. Laser irradiation induces the sulfidation of CuCoPBA, resulting in the formation of flower-like CuCoPBA-S. The growth of the flower-like CuCoPBA-S differs from CuCoPBA, which exhibits a nanocube morphology. Fig. 1b shows the Fourier transform infrared (FTIR) spectra of CuCoPBA and CuCoPBA-S. In the spectrum of CuCoPBA-S, the prominent peaks centered at ~3428, 3312, and 3202 cm^{-1} correspond to cobaltpentlandite (Co_9S_8). The peak positioned at ~2139 cm^{-1} is assigned to copper(I)thiocyanate (CuSCN). The presence of Co_9S_8 and Cu_2S is further confirmed by peaks positioned at ~1617 and 1401 cm^{-1}, and ~1096 and 700 cm^{-1}, respectively. Fig. 1c shows the Raman spectra of CuCoPBA and CuCoPBA-S. In the spectrum of CuCoPBA, the prominent peaks centered at 187.5 and 264.3 cm^{-1} are attributed to Cu–CN–Co deformation vibrations, whereas those at 489.3 and 524.2 cm^{-1} correspond to Cu–C and Co–C stretching vibrations. [50] The Raman spectrum of CuCoPBA-S exhibits peaks corresponding to the vibrations associated with Cu–S (177.8 cm^{-1}), Cu–C (489.3 cm^{-1}), Co–S (711.6 cm^{-1}), and CuSCN (2161.6 cm^{-1}). Although

View Article Online
DOI: 10.1039/D6IM00053C

with low intensity, peaks positioned at ~1399 and 1418 cm^{-1} are assigned to the stretching vibrations of Cu–N and Co–N, respectively. The Raman spectrum of CuCoPBA-S also exhibits characteristic peaks of pure sulfur powder in the range of 100–400 cm^{-1}, associated with the vibration of the S–S bond in the S8 species. [51] This shows that a small amount of pure sulfur is formed during the photoreduction process, which is further supported by the X-ray diffraction (XRD) analysis. Fig. S1 shows the XRD pattern of CuCoPBA and CuCoPBA-S. The XRD pattern of CuCoPBA exhibits major peaks positioned at 2θ values of 17.6°, 25.0°, 35.7°, 40.1°, 44.1°, 51.3°, 54.7°, and 57.9°, corresponding to (200), (220), (400), (420), (422), (440), (600), and (620), respectively (PDF#: 02-0169). After the formation of CuCoPBA-S, these peaks exhibit slight shifts. The XRD pattern of CuCoPBA-S appears complex owing to its ordered/disordered crystal structure, in which sulfidation results in the formation of individual sulfide phases on the PBA network, which is driven by the differences in their formation energies. Although the individual sulfide phases are structurally ordered, the entire CuCoPBA-S crystal structure is considered disordered. To quantitatively resolve the phase composition and structural characteristics of CuCoPBA-S, detailed Rietveld refinement analysis was performed. The refined XRD pattern of CuCoPBA-S is shown in Fig. S2. In addition to the parent CuCoPBA phase (PDF# 02-0169), the refinement confirms the formation of multiple sulfide-related phases, including CuSCN (PDF# 22-0253), Cu_2S (PDF# 12-0174), Co_9S_8 (PDF# 02-0169), and elemental sulfur (PDF# 08-0247). The presence of these phases substantiates the heterogeneous sulfidation process and supports the formation of an ordered/disordered CuCoPBA-S heterostructure. The refined lattice parameters, phase fractions, and reliability factors obtained from the Rietveld analysis are summarized in Table S1, providing quantitative validation of the phase evolution in CuCoPBA-S. The photoreduction of thiourea yields a small amount of elemental sulfur, which is unavoidable during the processing.

View Article Online
DOI: 10.1039/D6IM00053C

The XRD analysis reveals that the sulfidation process forms various sulfide compounds, such as CuSCN, Co_9S_8, and Cu_2S, within a PBA network. Fig. 1d shows the field-emission scanning electron microscopy (FESEM) images of CuCoPBA nanocubes at two different magnifications, along with FESEM–energy-dispersive X-ray spectroscopy (EDS) elemental mapping images for the N, C, Cu, and Co. Pulsed laser irradiation envisages the formation of CuCoPBA-S, with thiourea serving as the sulfur source. Fig. 1e shows the FESEM image of flower-like CuCoPBA-S and the corresponding FESEM–EDS elemental mapping for S, N, C, Cu, and Co. The FESEM–EDS elemental mapping confirmed the even distribution of sulfur throughout the material. The flower-like morphology of CuCoPBA-S, observed in the FESEM image results from the sulfidation of CuCoPBA, aided by thiourea as the sulfur precursor. Fig. 1f presents high-resolution transmission electron microscopy (HRTEM) images at different magnifications, verifying the flower-like morphology of CuCoPBA-S. High-magnification images reveal lattice fringes corresponding to Cu_2S and Co_9S_8, indicating that CuCoPBA-S exhibits a crystalline nature (ordered) within the PBA network structure (disordered). A lattice spacing of 0.314 nm (Cu_2S (111)) and 0.29 nm (Co_9S_8 (311)) are observed in the HRTEM images (selected region is given in yellow box) of CuCoPBA-S, as depicted in Fig. 1f.

View Article Online
DOI: 10.1039/D6IM00053C

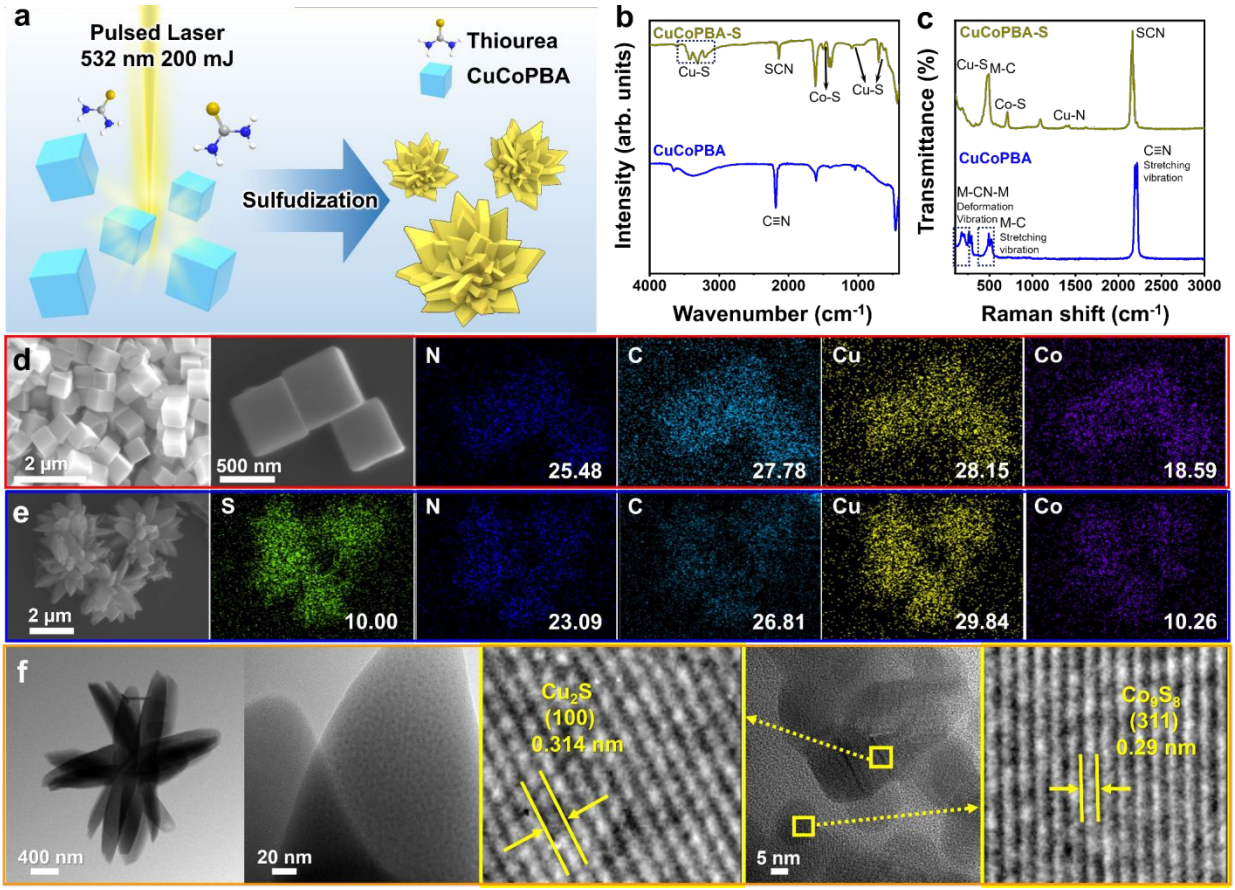

Fig. 1 (a) Schematic of CuCoPBA and CuCoPBA-S synthesis via pulsed laser irradiation; (b) FTIR spectra of CuCoPBA and CuCoPBA-S; (c) Raman spectra of CuCoPBA and CuCoPBA-S; (d) FESEM images of CuCoPBA with corresponding EDS elemental mapping; (e) FESEM image of CuCoPBA-S with corresponding EDS elemental mapping; (f) HRTEM images of CuCoPBA-S at different magnifications, high-resolution images showing lattice fringes corresponding to Cu_2S and Co_9S_8.

Surface chemical analysis of the CuCoPBA and CuCoPBA-S was performed using X-ray photoelectron spectroscopy (XPS). The XPS survey spectra obtained for CuCoPBA and CuCoPBA-S are depicted in Fig. 2a, confirming the presence of various elements in the samples. A small oxygen peak is observed, attributed to the inevitable formation of native oxide in the open environment. Fig. 2b shows the XPS C 1*s* deconvolution spectra for CuCoPBA and CuCoPBA-S.

View Article Online
DOI: 10.1039/D6IM00053C

In the CuCoPBA spectrum, a prominent peak positioned at 285.7 eV corresponds to the C–N bond, which diminishes in intensity in CuCoPBA-S owing to the ordered/disordered sulfidation process. Another peak positioned at 284.6 eV in the CuCoPBA spectrum, corresponding to the C–C bond, remains unaltered in CuCoPBA-S, though its intensity varies, indicating the structural integrity of the PBA network. Oxygen-containing surface functional groups are observed in both CuCoPBA and CuCoPBA-S, with peaks positioned at 287.3 and 288.8 eV corresponding to the C=O and O−C=O, respectively. Fig. 2c shows the XPS N 1*s* deconvolution spectra for CuCoPBA and CuCoPBA-S. In CuCoPBA, peaks at 397.60, 398.26, 399.11, and 399.92 eV are assigned to pyridinic-N, cyanide-N, pyrrolic-N, and C_3-N species, respectively. Upon sulfidation, the cyanide-N, pyridinic-N, and pyrrolic-N peaks shift slightly toward higher binding energies (398.34, 397.68, and 399.16 eV, respectively), indicating electronic redistribution around the nitrogen environment. Notably, the intensity of the cyanide-N peak decreases after sulfidation, while the pyridinic-N and pyrrolic-N contributions increase, suggesting partial disruption of the cyanide framework and the formation of defect-rich nitrogen environments. Meanwhile, the C_3-N peak exhibits increased intensity and shifts slightly toward lower binding energy (399.90 eV), reflecting rehybridization and structural rearrangement of nitrogen species. A peak corresponding to N–C_3 shifts from 400.0 eV in CuCoPBA to 400.8 eV in CuCoPBA-S, further evidencing changes in local nitrogen coordination. The Co 2*p* deconvoluted XPS spectra of CuCoPBA and CuCoPBA-S are shown in Fig. 2d. For CuCoPBA, the Co $2p_{3/2}$ and Co $2p_{1/2}$ peaks corresponding to mixed Co^{2+}/Co^{3+} states appear at 782.64/781.23 eV and 797.66/796.64 eV, respectively. After sulfidation, the Co^{3+}-related peaks in CuCoPBA-S shift to lower binding energies, appearing at 780.31 eV (Co $2p_{3/2}$) and 795.12 eV (Co $2p_{1/2}$), corresponding to an approximate negative shift of ~1.1 eV. This shift indicates increased electron density around Co centers due to the formation of Co–S bonds and altered

View Article Online
DOI: 10.1039/D6IM00053C

coordination environments. A similar trend is observed in the Cu 2*p* spectra (Fig. 2e). In CuCoPBA, Cu $2p_{3/2}$ peaks at 931.44 and 932.95 eV correspond to Cu^{+} and Cu^{2+} species, respectively, while Cu $2p_{1/2}$ peaks at 951.69 and 952.87 eV are also associated with Cu^{+} and Cu^{2+} states. In CuCoPBA-S, the Cu^{+}-related peaks shift to lower binding energies, appearing at 930.17 eV (Cu $2p_{3/2}$) and 950.19 eV (Cu $2p_{1/2}$), representing a negative shift of approximately 1.5 eV. This behavior suggests partial reduction of Cu species and enhanced electron donation upon sulfidation. Fig. 2f shows the S 2*p* spectra for CuCoPBA and CuCoPBA-S. No sulfur peaks are observed in CuCoPBA, as it lacks sulfur content, but in the spectra of CuCoPBA-S, peaks located at 163.5, 162.9, and 162.1 eV correspond to C–S–C, Co–S, and Cu–S, respectively.

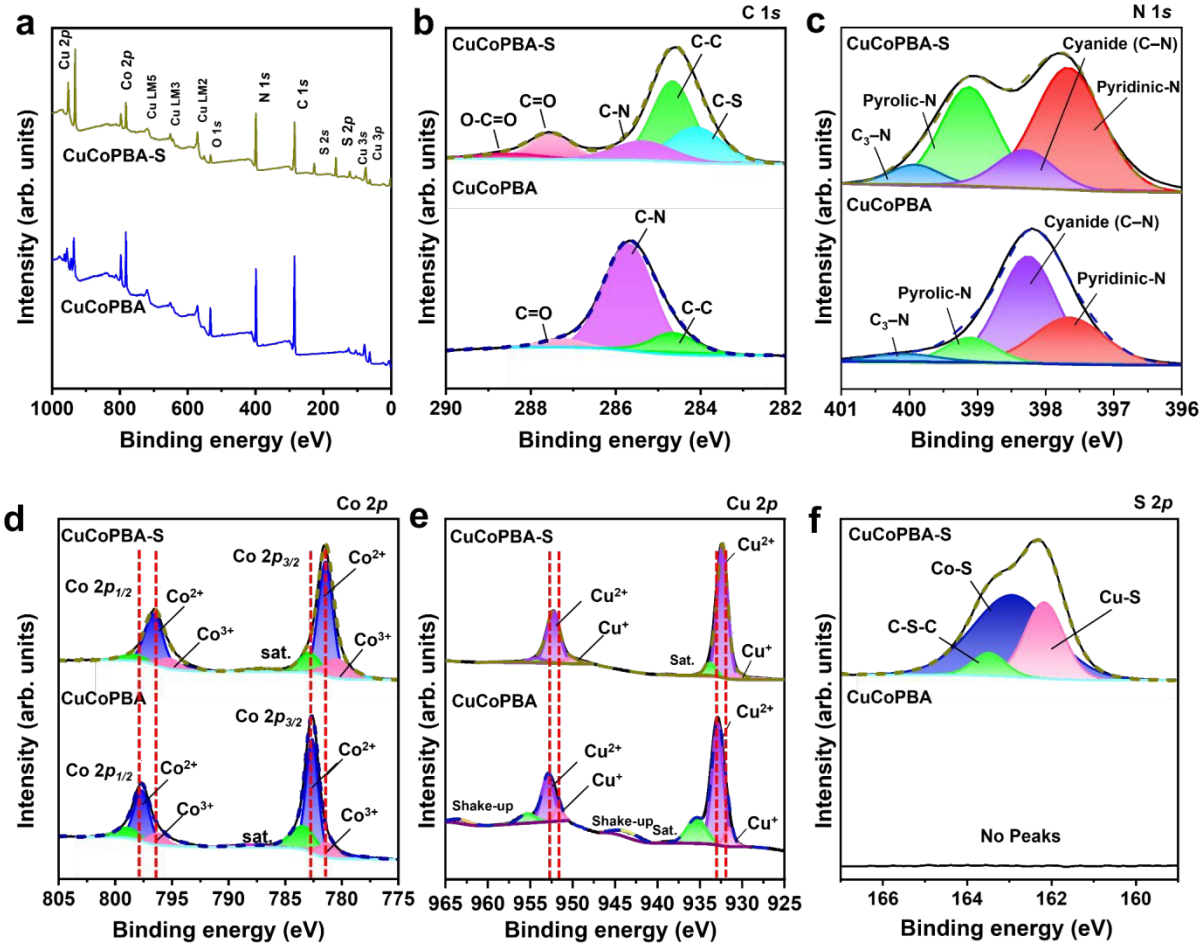

View Article Online
DOI: 10.1039/D6IM00053C

Fig. 2 (a) XPS survey spectra of CuCoPBA and CuCoPBA-S. XPS deconvolution spectra of CuCoPBA and CuCoPBA-S for (b) C 1*s*, (c) N 1*s*, (d) Co 2*p*, (e) Cu 2*p*, and (f) S 2*p*.

2.2 *In situ* Raman analysis of CuCoPBA-S via acoustic levitation

In situ Raman spectroscopic analysis, coupled with acoustic levitation, investigated the ordered/disordered structural formation of the CuCoPBA-S. The left panel of Fig. 3a shows a digital photograph of the water droplet (reactant) ready for acoustic levitation, irradiated with a 532-nm laser at a power of 100 mJ. Upon laser irradiation, CuCoPBA and thiourea reacted to form the ordered/disordered flower-like CuCoPBA-S structure. The right panel of Fig. 3a depicts the digital photograph of the laser-irradiated CuCoPBA-S, showing a decrease in the size of the reactant droplet. During the laser irradiation, *in situ* Raman spectroscopy recorded structural changes in CuCoPBA-S at 1-min intervals for continuous 12 min, with the resulting contour plots depicted in Fig. 3b. A detailed investigation of the formation of the ordered/disordered flower-like CuCoPBA-S was performed via *in situ* Raman spectroscopy, with data collected at 1-min intervals for 12 min. From Fig. 3c, the formation of Cu(SCN) is observed during the first 1 min 20 s, indicated by the increased intensity peaks at 2161.6 cm^{-1}. Immediately after 1 min 20 s, the formation of Cu_2S became dominant, as indicated by the increase in its peak intensity at 177.8 cm^{-1}, which continued to increase, reaching saturation by 3 min 45 s. Finally, the formation of Co_9S_8 became prominent, as evidenced by the increase in peak intensity at 711.6 cm^{-1}. The *in situ* Raman spectroscopic analysis, coupled with acoustic levitation, reveals that the formation of the ordered/disordered CuCoPBA-S structure is time dependent. The enthalpy of formation for each sulfur-based compound differs as it is associated with the thermochemical properties of the compounds. [52] The flower-like morphology of CuCoPBA-S results from the different enthalpy of formation, determining the sulfidation reaction with the metal atoms, leading to the sequential

View Article Online
DOI: 10.1039/D6IM00053C

formation of Cu(SCN), Cu_2S, and Co_9S_8. This provides insights into the bottom-up synthesis of CuCoPBA-S in an ordered/disordered manner through a time-dependent sulfidation reaction.

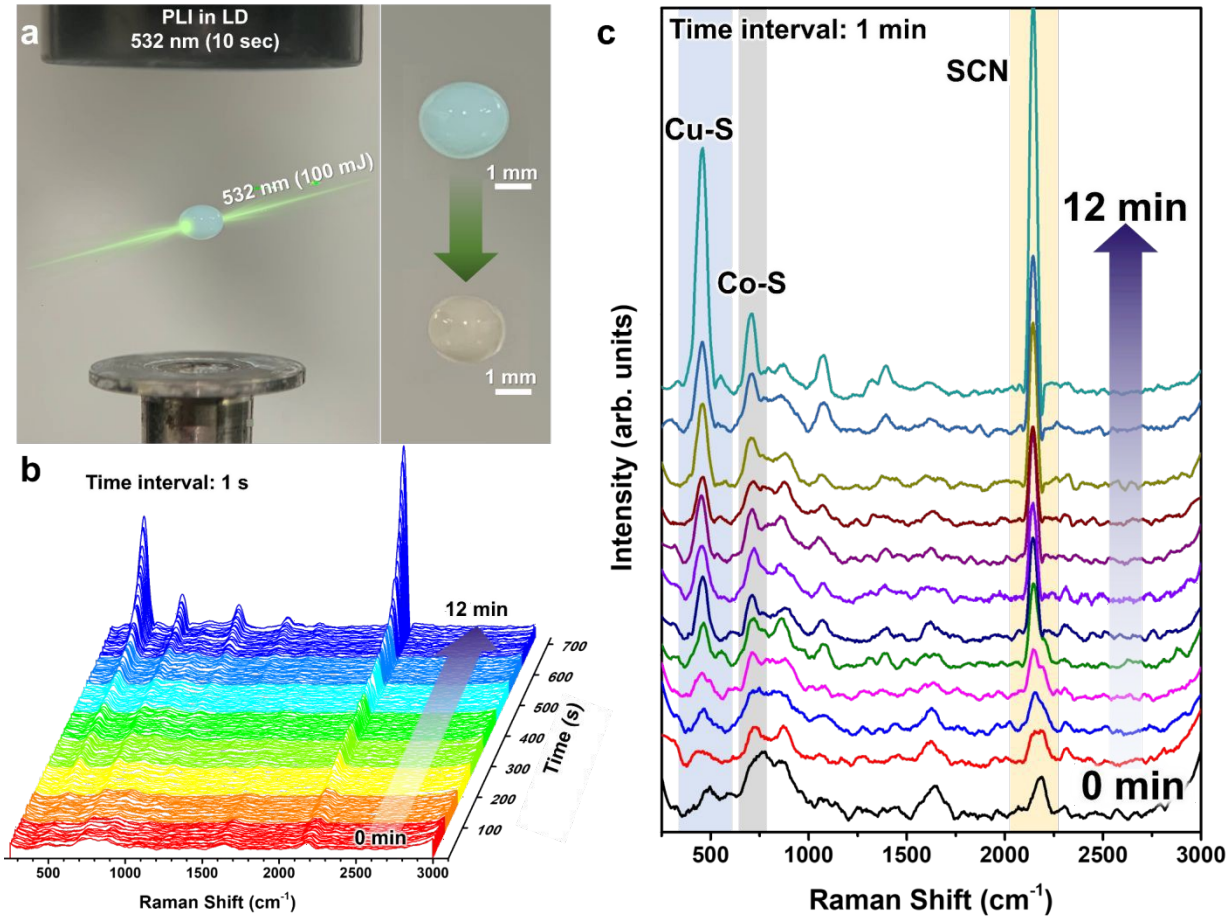

Fig. 3 (a) Digital photograph of the acoustic levitated droplet (LD) under laser irradiation (left panel) and the water droplet after the formation of CuCoPBA-S (right panel); (b) *in situ* Raman contour plots of CuCoPBA-S over a 12-minute reaction period, and (c) *in situ* Raman spectra of CuCoPBA-S.

2.3 Electrocatalytic NO_2RR (eNO_2RR) performance evaluation

The electrocatalytic performance of the CuCoPBA and CuCoPBA-S was evaluated using a standard H-cell in a three-electrode configuration, as shown schematically in Fig. 4a. The

View Article Online
DOI: 10.1039/D6IM00053C

electrocatalyst material (CuCoPBA and CuCoPBA-S) coated carbon cloth served as the working electrode, the graphite rod as the counter electrode, Hg/HgO as the reference electrode, Nafion membrane as the electrolyte separator, 1 M KOH as the anolyte, and 1.0 M KOH + 0.1 M KNO_2 as the catholyte. Fig. 4b shows the linear sweep voltammetry (LSV) curves of the CuCoPBA and CuCoPBA-S obtained in a 1.0 M KOH electrolyte, with and without the addition of 0.1 M KNO_2. The LSV curves reveal that both catalysts exhibit high current densities within a reduction potential range of 0.0 to −0.6 V vs. reversible hydrogen electrode (RHE) when NO_2^- is present in the electrolyte, suggesting their potential for the eNO_2RR. A noticeable variation in the LSV curve for the CuCoPBA-S shows a more positive onset potential and higher current density compared to CuCoPBA. Notably, the eNO_2RR performance of CuCoPBA-S is much higher than that of CuCoPBA, as evidenced by the LSV curves. However, at highly negative potentials, the current density for CuCoPBA-S exceeds that of CuCoPBA owing to the slower reaction kinetics of CuCoPBA, as reflected in the Tafel slopes (Fig. 4c) and Nyquist plots (Fig. 4d). In addition, the Nyquist plot for the CuCoPBA and CuCoPBA-S obtained in the 1.0 M KOH electrolyte, with and without 0.1 M KNO_2, displays lower ohmic resistance for CuCoPBA-S compared to CuCoPBA, attributed to the higher ionic conductivity of the CuCoPBA-S. The charge transfer resistance (R_{ct}) for CuCoPBA-S is lower than that for CuCoPBA, confirming enhanced conductivity of CuCoPBA-S after sulfidation, likely owing to the creation of additional ionic channels that facilitate the easy penetration of electrolyte ions into the inner pores of the catalyst electrode, thereby enhancing the catalytic activity of CuCoPBA-S. FESEM analysis further reveals that CuCoPBA-S has a larger active surface area compared to CuCoPBA. This increase in surface area contributes to the enhanced catalytic activity of CuCoPBA-S. Moreover, the flower-like

View Article Online
DOI: 10.1039/D6IM00053C

morphology of CuCoPBA-S aids in the easy penetration of electrolyte ions, as the pores of the electrode nanostructure are more favorable for ion diffusion into the inner pores.

The cyclic voltammetry (CV) curves of the CuCoPBA and CuCoPBA-S, measured in the range of −0.1 to 1.1 V vs. RHE at 50 mV s^{-1} in 1 M KOH electrolyte (Fig. S3), show a large area under the curve for the CuCoPBA-S. The active sites were calculated as 1.85×10^{-7} and 2.31×10^{-6} mol cm^{-2} for CuCoPBA and CuCoPBA-S, respectively. This indicates that the CuCoPBA-S achieves a superior eNO_2RR activity compared with CuCoPBA, which can be further verified by turnover frequency (TOF), as depicted in Fig. S4. TOF, which reflects the efficiency of the catalyst for eNO_2RR, was 0.004, 0.006, and 0.042 s^{-1} for CuCoPBA at different reduction potentials of −0.4, −0.5, and −0.6 V, respectively. By contrast, CuCoPBA-S showed a rapid increase in TOF, with 0.042, 0.083, and 0.232 s^{-1} at −0.4, −0.5, and −0.6 V, respectively. These higher TOFs suggest that the CuCoPBA-S exhibits superior efficiency toward eNO_2RR. The CV curves in the non-Faradaic potential region (0.65–0.70 V vs. RHE) at various scan rates in the 1 M KOH electrolyte, as shown in Fig. S5, reveal that the CuCoPBA-S has a large area under the curve than CuCoPBA, indicating a higher electrochemical activity. The double-layer capacitance (C_{dl}) for CuCoPBA and CuCoPBA-S, calculated from Fig. S6, of 58 and 354 mF cm^{-2}, respectively, further confirms the superior electrochemical activity of the CuCoPBA-S.

After the eNO_2RR, quantitative analysis of the reaction products—including nitrogen (N_2), hydrogen (H_2), and NH_3—was carried out. The YR (NH_3) and FE (NH_3) of both CuCoPBA and CuCoPBA-S were evaluated at different applied reduction potentials. The YR (NH_3) was determined using the indophenol blue method in conjunction with UV–vis absorption spectroscopy. The corresponding UV–vis spectra (Fig. S7a) and calibration curves (Fig. S7b) for NH_4^+ were derived from the absorbance of NH_4Cl standard solutions with known concentrations.

View Article Online
DOI: 10.1039/D6IM00053C

The eNO_2RR catalysis was conducted for 1 h, and the concentration of NH_4^+ was determined every 15 min. To verify that the detected NH_4^+ originated exclusively from NO_2^- reduction rather than from extraneous nitrogen sources, a control experiment was performed in 1.0 M KOH electrolyte without the addition of KNO_2, under otherwise identical electrolysis conditions. The current profiles recorded at different applied potentials are shown in Fig. S8a. Importantly, the corresponding UV–Vis absorption spectra (Fig. S8b) exhibit no detectable changes across the tested potentials, confirming that NH_4^+ formation occurs solely from the electrochemical reduction of NO_2^-. Fig. 4e shows the variation in FE (NH_3) with respect to the reduction potential for the CuCoPBA and CuCoPBA-S. For CuCoPBA, FE (NH_3) values of 27.91%, 41.28%, 45.55%, 39.13%, and 29.41% are obtained at −0.3, −0.4, −0.5, −0.6, and −0.7 V vs. RHE, respectively. In contrast, CuCoPBA-S exhibits significantly higher FE (NH_3) values of 31.15%, 60.24%, 80.91%, 57.98%, and 44.71% at the corresponding potentials. In both cases, FE (NH_3) values increase with increasing cathodic potential from −0.3 to −0.5 V vs. RHE, followed by a decline at more negative potentials. This decrease is attributed to the enhanced contribution of competing side reactions, such as the HER, at higher overpotentials. The maximum FE (NH_3) value for CuCoPBA is 45.55% at −0.5 V versus RHE, whereas CuCoPBA-S achieves a significantly higher FE (NH_3) value of 80.91% under the same conditions. Accordingly, −0.5 V vs. RHE was selected as the optimal operating potential for subsequent electrochemical measurements. The electrocatalytic performance of CuCoPBA-S, evaluated in terms of YR (NH_3), is compared with that of representative catalysts reported in the literature in Table S2. This benchmarking analysis demonstrates that CuCoPBA-S outperforms many previously reported systems, highlighting its strong potential and competitiveness for eNO_2RR. The NH_3 quantification was further confirmed using NMR spectroscopy at different reduction potentials. To determine the NH_4^+ concentration

View Article Online
DOI: 10.1039/D6IM00053C

during the conversion of NO_2^- to NH_4^+, ^1H NMR analysis was performed using $^{14}NH_4^+$ as the feedstock. The NMR spectra and calibration curves are depicted in Fig. S9. Electrolysis was evaluated at −0.5 V in a 0.5 M $^{14}NO_2^-$ electrolyte, and the collected electrolyte showed standard triplet peaks for $^{14}NH_4^+$ in the spectra (Fig. 4g). ^1H NMR spectra obtained for CuCoPBA and CuCoPBA-S at different reduction potentials for NH_3quantification are shown in Fig. S10. A comparison of the FE (NH_3) for CuCoPBA and CuCoPBA-S, calculated from UV-Vis absorption spectroscopy and ^1H NMR spectroscopy at different reduction potentials, is presented in Fig. S11. The FE (NH_3) for CuCoPBA from ^1H NMR analysis was found to be 30.71%, 42.83%, 47.65%, 41.30%, and 30. 22% at −0.3, −0.4, −0.5, −0.6, and −0.7 V vs. RHE, respectively. Similarly, the FE (NH_3) for CuCoPBA-S from ^1H NMR analysis was found to be 31.03%, 62.22%, 83.03%, 58.03%, and 44.54% at −0.3, −0.4, −0.5, −0.6, and −0.7 V vs. RHE, respectively. These data show no significant difference in the FE (NH_3) values obtained for CuCoPBA and CuCoPBA-S when calculated from UV-Vis and ^1H NMR spectra. The YR (NH_3) calculated from UV-Vis spectroscopic analysis at different reduction potentials for both electrocatalysts is depicted in Fig. 4f. In both cases, the YR (NH_3) increases with highly negative reduction potentials; however, CuCoPBA-S exhibits a sudden increase compared with CuCoPBA. The CuCoPBA-S exhibits a higher YR (NH_3) (3394.1 μg h^{-1} cm^{-2}) than CuCoPBA (756.7 μg h^{-1} cm^{-2}) at −0.5 V vs. RHE. Furthermore, the YR (NH_3) steadily increased at highly negative potentials, reaching values of 577.5 μg h^{-1} cm^{-2} for the CuCoPBA-S and 2570.9 μg h^{-1} cm^{-2} for CuCoPBA at −0.7 V vs. RHE. The YR (NH_3) obtained for CuCoPBA and CuCoPBA-S at different reduction potentials, expressed in μmol h^{-1} cm^{-2} is shown in Fig. S12. Fig. S13 shows the gravimetric YR (NH_3) of CoCuPBA and CuCoPBA-S at different reduction potentials, expressed in μmol h^{-1} mg_{cat}^{-1}. The YR (NH_3) obtained for CuCoPBA and CuCoPBA-S is further compared with data from ^1H NMR

View Article Online
DOI: 10.1039/D6IM00053C

analysis. The area-specific YR (NH_3) obtained from UV-Vis and NMR analyses for CuCoPBA and CuCoPBA-S at different reduction potentials, expressed in μg h^{-1} cm^{-2} and μmol h^{-1} cm^{-2} are shown in Fig. S14 and Fig. S15, respectively. Fig. S16 compares the FE (NH_3) expressed in μmol h^{-1} mg_{cat}^{-1}, calculated from UV-Vis and ^1H NMR spectra for the CuCoPBA and CuCoPBA-S at different reduction potentials. These data show no significant difference in the YR (NH_3) values obtained for CuCoPBA and CuCoPBA-S when calculated from UV-Vis and ^1H NMR spectra. Further, N_2 and H_2 were also quantified by gas chromatography. During the analysis, no detectable N_2 was found at any reduction potential. However, H_2 was systematically quantified for both catalysts, CuCoPBA and CuCoPBA-S, at different reduction potentials. Fig. S17 shows the FE (H_2) and YR (H_2) calculated for CuCoPBA and CuCoPBA-S at different reduction potentials. Fig. S17a shows the variation in FE (H_2) and YR (H_2) with reduction potential for CuCoPBA. FE (H_2) values of 2.38%, 2.64%, 6.14%, 22.52%, and 36.94% were achieved at −0.3, −0.4, −0.5, −0.6, and −0.7 V vs. RHE, respectively. Similarly, YR (H_2) values of 6.82, 8.31, 6.29, 52.01, and 141.38 μmol h^{-1} cm^{-2} were achieved at −0.3, −0.4, −0.5, −0.6, and −0.7 V vs. RHE, respectively. For CuCoPBA-S (Fig. S17b), the FE (H_2) was found to be 3.05%, 3.56%, 3.61%, 14.61%, and 24.33% at −0.3, −0.4, −0.5, −0.6, and −0.7 V vs. RHE, respectively. Similarly, YR (H_2) values of 6.79, 8.32, 12.21, 42.01, and 115.38 μmol h^{-1} cm^{-2} were achieved at −0.3, −0.4, −0.5, −0.6, and −0.7 V vs. RHE, respectively. Overall, a lower YR (H_2) was observed for CuCoPBA-S compared to CuCoPBA. While the present study focuses on intrinsic catalytic activity in a conventional three-electrode configuration, evaluating NO_2^- reduction in a flow-cell system represents an important step toward practical implementation. Flow cells can significantly enhance mass transport, enabling operation at higher current densities and improved reactant utilization under continuous conditions. Given the porous architecture and high surface area of the developed catalyst, it is

View Article Online
DOI: 10.1039/D6IM00053C

expected to perform favorably in flow-cell configurations, where efficient electrolyte permeation and reactant accessibility are critical. Future studies will therefore focus on integrating the catalyst into gas-diffusion or flow-through electrodes to assess performance under industrially relevant conditions, including high current density operation, long-term stability, and NH_3 production rates.

The enhanced eNO_2RR performance of CuCoPBA-S is likely due to the greater availability of accessible active sites for interaction with the electrolyte compared to CuCoPBA, which facilitates more efficient catalytic processes. In general, the surface area of a catalyst is a key factor governing its activity, as materials with larger surface areas typically provide more active sites and thus exhibit improved catalytic performance relative to those with smaller surface areas. To investigate the role of surface area in influencing eNO_2RR activity, Brunauer–Emmett–Teller (BET) surface area measurements were conducted for both CuCoPBA and CuCoPBA-S. Fig. S18 shows the N_2-sorption isotherms of CuCoPBA and CuCoPBA-S. From these adsorption-desorption data, the BET surface areas for CuCoPBA and CuCoPBA-S were calculated to be5.38 and 3.78 $m^2\ g^{-1}$, respectively. This result indicates that the enhanced catalytic activity of CuCoPBA-S is not primarily due to its surface area, as CuCoPBA actually exhibits a larger BET surface area. Instead, the origin of the activity is attributed to the active sites of CuCoPBA-S, which will be further elucidated with the help of DFT predictions, *in situ* Raman, and *ex situ* FTIR analyses in forthcoming sections. To investigate the long-term stability of CuCoPBA-S, electrolysis was performed for 10 h, with YR (NH_3) and FE (NH_3) calculated each hour. The electrochemical stability of CuCoPBA-S for eNO_2RR was recorded over 10 consecutive cycles at −0.5 V vs. RHE (each cycle lasting 1 h with electrolyte replacement after each cycle). No profound variation in UV-Vis absorbance was observed after 10 cycles, indicating excellent cyclic stability of the CuCoPBA-S for eNO_2RR. The variation in the YR (NH_3) and FE (NH_3) (Fig. 4h) indicates

View Article Online
DOI: 10.1039/D6IM00053C

no substantial variation after 10 h of cycling. To elucidate possible structural and morphological changes of the catalyst electrode (CuCoPBA-S coated on carbon cloth) after cycling, post-stability characterizations were carried out using FESEM imaging, SEM-EDS elemental mapping, *ex situ* XRD, and *ex situ* XPS analyses. Fig. S19 compares FESEM images and SEM–EDS maps of the CuCoPBA-S electrode before and after the stability test. No discernible morphological changes are observed after cycling, and the characteristic flower-like morphology is well preserved. Moreover, SEM–EDS elemental mapping confirms a uniform distribution of the constituent elements both before and after cycling, demonstrating that the catalyst remains compositionally homogeneous during prolonged operation. Fig. S20 shows the XRD patterns of the CuCoPBA-S electrode before and after the stability test. A broad diffraction peak at 25.82° is observed in both patterns and is attributed to the C(002) plane of the carbon cloth substrate. No additional phase formation or peak shift is detected after cycling, indicating preserved crystallographic integrity. XPS analyses were further performed to probe surface chemical stability. The deconvoluted C 1*s* spectra before and after cycling (Fig. S21) display peaks at 284.01, 284.83, 285.85, and 287.81 eV, corresponding to C-C, C-N, C=O, and O-C=O species, respectively, with no appreciable shifts after the stability test. Similarly, the N 1*s* spectra (Fig. S22) show peaks at 397.97, 398.84, 399.47, and 400.17 eV, assigned to pyridinic-N, cyanide-N, pyrrolic-N, and C_3-N species, respectively, which also remain unchanged after cycling. The Co 2*p* spectra (Fig. S23) exhibit Co $2p_{3/2}$ peaks at 780.66 and 782.07 eV corresponding to Co^{3+} and Co^{2+}, and Co $2p_{1/2}$ peaks at 796.21 and 797.08 eV corresponding to Co^{3+} and Co^{2+}, respectively. No binding energy shifts are observed after the stability test. Likewise, the Cu 2*p* spectra before and after cycling (Fig. S24) show Cu $2p_{3/2}$ peaks at 931.35 and 932.62 eV (Cu^{+} and Cu^{2+}) and Cu $2p_{1/2}$ peaks at 950.96 and 952.22 eV (Cu^{+} and Cu^{2+}), with no significant changes after 10-hours of operation. The deconvoluted S 2*p* spectra (Fig.

View Article Online
DOI: 10.1039/D6IM00053C

S25) display peaks at 162.45, 163.46, and 164.31 eV corresponding to Cu–S, Co–S, and C–S–C species, respectively. After cycling, these peaks shift slightly to lower binding energies (162.01, 163.28, and 164.29 eV), indicating minor electronic redistribution at sulfur sites. In addition, weak peaks at 168.91 and 170.29 eV are observed and assigned to C–SO_3[53] and Cu–S–O species, [54] respectively, which are attributed to partial reduction or decomposition of Nafion on the catalyst electrode during prolonged electrolysis.

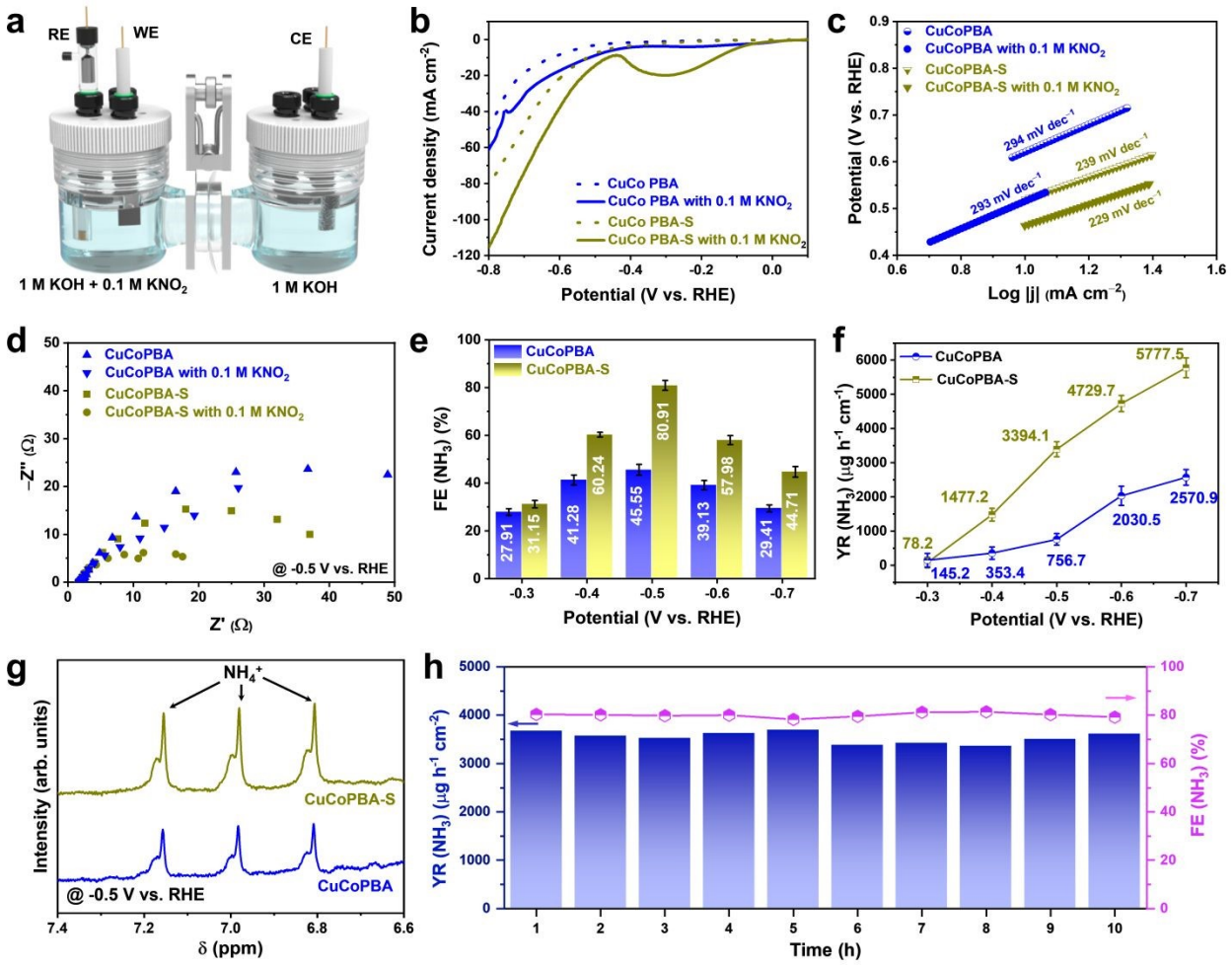

Fig. 4 Electrocatalytic performance of CuCoPBA and CuCoPBA-S for eNO_2RR in 1 M KOH electrolyte. (a) schematic diagram of the H-cell setup for eNO_2RR testing; (b) LSV profiles recorded with and without 0.1 M KNO_3; (c) Tafel plots; (d) Nyquist plots; (e) comparison of the

View Article Online
DOI: 10.1039/D6IM00053C

FE (NH_3) for the CuCoPBA and CuCoPBA-S at various reduction potentials; (f) comparison of YR (NH_3) for CuCoPBA and CuCoPBA-S at various reduction potentials; (g) ^{1}H NMR spectrum of the catholyte after 60 min of the eNO_2RR at −0.5 V vs. RHE; (h) Variation in the YR (NH_3) and FE (NH_3) over 10 consecutive cycles at −0.5 V vs. RHE.

2.4 *In situ* and *ex situ* analysis of CuCoPBA-S for eNO_2RR

To elucidate the origin of catalytic activity and identify reaction intermediates on CuCoPBA-S during the eNO_2RR, *in situ* Raman spectroscopy and *ex situ* FTIR analyses were performed. A schematic illustration of the *in situ* Raman setup is shown in Fig. 5a, with a digital photograph of the experimental configuration provided in Fig. S26. The *in situ* Raman spectra of CuCoPBA-S collected at OCP and at applied potentials ranging from −0.2 to −0.7 V vs. RHE, are presented in Fig. 5b. Two broad bands centered at approximately 1348 and 1610 cm^{-1}, corresponding to the D and G bands of the carbon cloth substrate, are consistently observed across all spectra. A characteristic peak at ~1250 cm^{-1}, assigned to NO_2^- species, appears at all tested potentials, confirming the presence and electrochemical consumption of NO_2^- during reduction. Upon applying a cathodic potential of −0.2 V vs. RHE, new Raman features emerge at approximately 940 and 1500 cm^{-1}, which are attributed to the *NH_2OH intermediate and NH_3 product vibrations, respectively.[55, 56] In addition, a shoulder near ~1220 cm^{-1} develops under cathodic bias and is assigned to surface-adsorbed *NO_2 species. This feature initially intensifies and then diminishes at more negative potentials, indicating rapid conversion of *NO_2 intermediates and fast eNO_2RR kinetics, as further evidenced in Fig. S27. To probe solution-phase intermediates and products, *ex situ* ATR–FTIR spectroscopy was conducted on catholyte samples collected after 1 h of eNO_2RR at OCP and at applied potentials between −0.2 and −0.7 V vs. RHE. The potential-dependent ATR–FTIR spectra (Fig. 5c) and corresponding contour plots (Fig. 5d and 5e) reveal several bands that increase in intensity with increasing cathodic bias. Distinct absorption features at ~1095 and 1236

View Article Online
DOI: 10.1039/D6IM00053C

cm^{-1} are assigned to *NH_2OH and *NH_2 vibrations, respectively, while the band at 1640 cm^{-1} and the broad feature centered at 3368 cm^{-1} are attributed to the *NO intermediate and the NH_3 product. Collectively, the *in situ* Raman and *ex situ* ATR–FTIR results support a stepwise eNO_2RR pathway on CuCoPBA-S involving *NO, *NH_2OH, and *NH_2 as key intermediates en route to NH_3 formation.[57] To demonstrate practical conversion of the produced NH_3 into a value-added product, an acid-trap method was employed to convert NH_3 into ammonium chloride (NH_4Cl). A schematic illustration of the NH_3-to-NH_4Cl conversion setup is shown in Fig. 5f. After eNO_2RR catalysis, the catholyte was collected and heated at 70 °C under argon purging to release dissolved NH_3 gas. The evolved NH_3 was subsequently passed through an acid trap containing 2 M HCl, where it was quantitatively converted into NH_4Cl. The successful formation of NH_4Cl was confirmed by XRD analysis (Fig. 5g), with diffraction peaks in good agreement with the standard reference pattern (PDF# 04-0836). A digital photograph of the NH_4Cl product obtained after the acid-trap process is shown as an inset in Fig. 5g. These results highlight the mechanistic understanding and practical relevance of CuCoPBA-S for eNO_2RR and underscore its potential for future electrocatalytic NH_3 manufacturing and nitrogen upcycling applications.

View Article Online
DOI: 10.1039/D6IM00053C

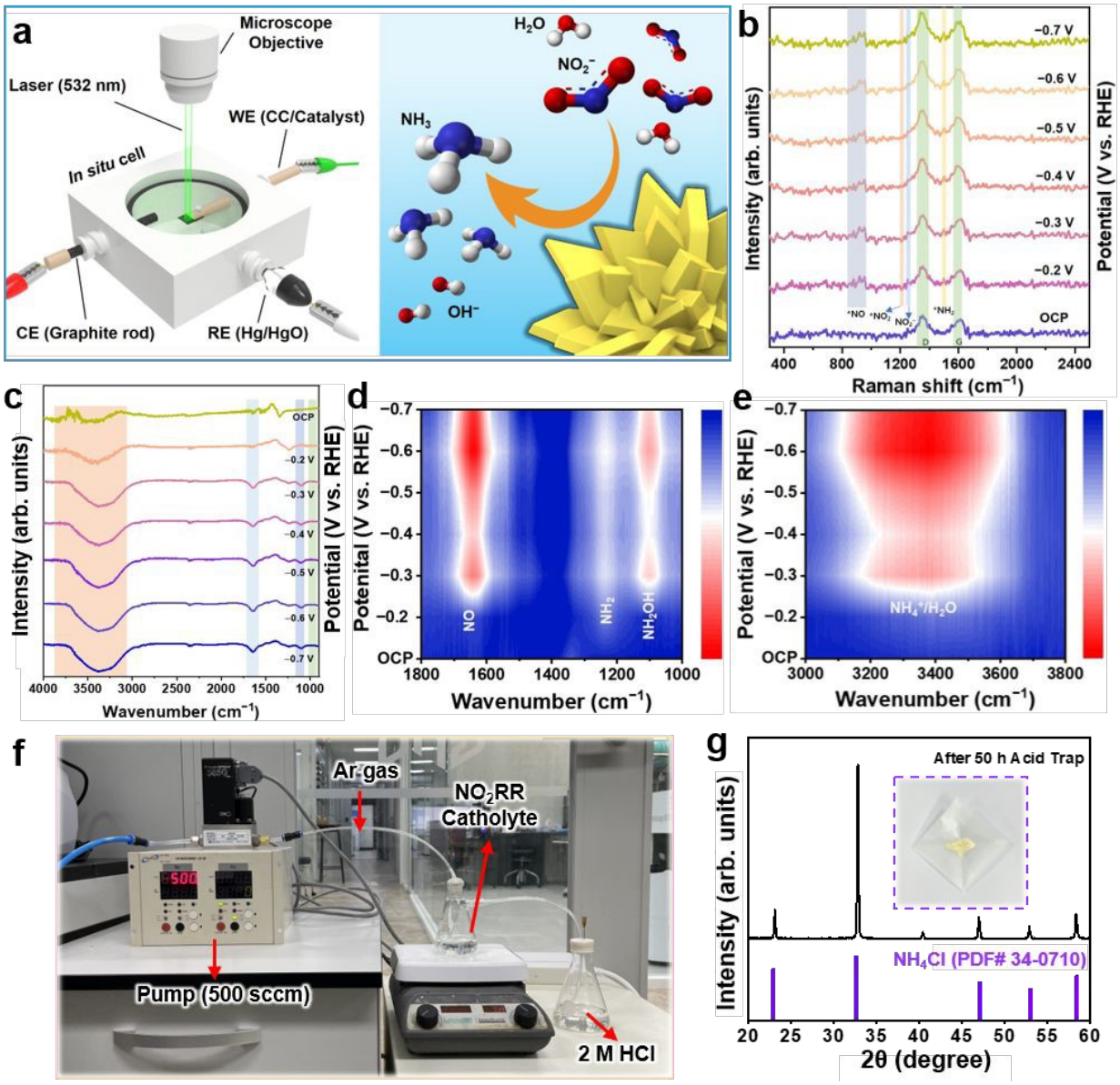

Fig. 5 (a) Schematic depiction of the *in situ* Raman experimental setup; (b) *in situ* Raman spectra recorded during the NO_3RR using the CuCoPBA-S at different reduction potentials; (c) *ex situ* FTIR spectra and (d, e) contour plots of the catholyte collected after 1 h NO_3RR using the CuCoPBA-S at different reduction potentials; (f) schematic of the acid-trap experiment for real-time production of NH_4Cl after the eNO_2RR using the CuCoPBA-S; (g) XRD spectra of NH_4Cl after the eNO_2RR using the CuCoPBA-S (Inset: Digital image of NH_4Cl collected in a weighing paper after acid-trap).

View Article Online
DOI: 10.1039/D6IM00053C

2.5 Density functional theory calculations

Theoretical density functional theory (DFT) calculations were performed to understand the mechanisms and pathways of the CuCoPBA and CuCoPBA-S during eNO_2RR. All first-principles DFT calculations are carried out using the Quantum ESPRESSO (QE) package with a plane-wave pseudopotential framework. The studied systems included CuCoPBA, Cu_2S, Co_9S_8, and CuCoPBA-S. The CuCoPBA-S heterostructure is constructed using 2×2×1, 4×4×1, and 3×3×1 supercell of CuCoPBA, Cu_2S, and Co_9S_8 was used, respectively. The coupling between Co-S, and Cu-S is considered in the construction of the CuCoPBA-S. The surfaces of CuCoPBA, Cu_2S, and Co_9S_8 were arranged in a stacked configuration along the x-axis with respect to the (001) plane, which was expected to enhance the visibility of additional active sites for eNO_2RR. However, there is little variation in the typical lattice structures of CuCoPBA, Cu_2S, and Co_9S_8 along all axes. Consequently, a 1% strain is applied to both Cu_2S and Co_9S_8. The exchange-correlation energy is described using the Perdew-Burke-Ernzerhof (PBE) functional in the generalized gradient approximation (GGA), and core-electron interactions are represented by ultrasoft pseudopotentials. The DFT-optimized side-view and top-view of the crystal structures for Cu_2S, Co_9S_8, and CuCoPBA are shown in Fig. S28-30, respectively. The side and top views of the CuCoPBA-S crystal structure are shown in Fig. S31, Fig. 6a and 6b, respectively. Charge distribution profiles for Cu_2S, Co_9S_8, CuCoPBA, and CuCoPBA-S are shown in Fig. S32-35, respectively, with CuCoPBA-S displaying a higher charge distribution, facilitating fast electron transfer during eNO_2RR. The valence electron distribution (Fig. S36) for Cu_2S, Co_9S_8, CuCoPBA, and CuCoPBA-S shows that CuCoPBA-S has more spatially distributed valence electrons than CuCoPBA, thereby enhancing electron transport. This peculiar electronic structure benefits charge transfer during catalysis, resulting in enhanced conductivity and efficiency. The total density of

View Article Online
DOI: 10.1039/D6IM00053C

states (DOS) diagrams for Cu_2S, Co_9S_8, CuCoPBA, and CuCoPBA-S are shown in Fig. S37, with CuCoPBA-S exhibiting a higher DOS than other materials, indicating greater carrier concentration and more favorable electron energy distributions in the material. The partial DOS (PDOS) for Cu_2S and Co_9S_8 given in Fig. S38a and S38b, respectively, show continuous and more broader bands for Co_9S_8 compared with Cu_2S, whereas the PDOS for CuCoPBA (Fig. 6c) and CuCoPBA-S (Fig. 6d) shows that CuCoPBA-S has broader electronic states than CuCoPBA. The energy-band diagrams of Cu_2S (Fig. S39a), Co_9S_8 (Fig. S39b), CuCoPBA (Fig. 6e), and CuCoPBA-S (Fig. 6f) further confirm that the CuCoPBA-S possesses stronger the conduction and valence bands crossing near the Fermi level, representing superior electronic conductivity. Two possible pathways for the reduction of NO_2^- to NH_3 are outlined. The incorporation of sulfur into the structure of CuCoPBA during the sulfidation procedure modulates the electronic structure of the Co site of CuCoPBA in CuCoPBA-S, thereby boosting eNO_2RR by effectively capturing the NO_3^- on the CuCoPBA-S surface. DFT-optimized crystal structure of CuCoPBA/Cu_2S/Co9S8 is shown in Fig. 6g and the adsorption energy for NO_2^-at various sites of CuCoPBA/Cu_2S/Co_9S_8 is calculated. The adsorption configurations of NO_2^- at different interfacial metal sites in the CuCoPBA/Cu_2S/Co_9S_8 heterostructure were systematically investigated by DFT calculations. Specifically, NO_2^- adsorption at (i) the Cu site of Cu_2S at the CuCoPBA/Cu_2S/Co_9S_8 interface, (ii) the Co site of Co_9S_8 at the same interface, (iii) the bimetallic Co–Cu interfacial site of CuCoPBA/Cu_2S/Co_9S_8, (iv) the Co-site of CuCoPBA at the interface, and (v) the Cu site of CuCoPBA at the interface are shown in Fig. 6h-l, respectively. The corresponding adsorption energies (E_{ads}) are −1.49, −1.57, −1.96, −1.24, and −1.24 eV, respectively. Among these configurations, NO_2^- adsorption at the Cu site of Cu_2S and the Co site of Co_9S_8 at the CuCoPBA/Cu_2S/Co_9S_8 interface exhibits the most negative adsorption energy, indicating the most favorable adsorption for initiating eNO_2RR.

View Article Online
DOI: 10.1039/D6IM00053C

Notably, bidentate adsorption of NO_2^- across interfacial Co–Cu dual sites is thermodynamically more favorable than monodentate adsorption on isolated Cu or Co sites. This enhanced stability arises from stronger interfacial bonding, improved electron transfer, and more optimal intermediate energetics, all of which collectively enhance the kinetics and selectivity of NO_2^- reduction to NH_3. Hence, DFT calculations further reveal that the superior eNO_2RR activity of the Co–Cu interfacial sites originates from energetically favorable bidentate NO_2^- adsorption compared with single-metal adsorption behavior. Charge density difference analysis confirms pronounced charge redistribution between the dual-metal sites and the adsorbed NO_2^- species, indicating efficient electron donation into the antibonding orbitals of NO_2^-. This electron transfer weakens and elongates the N–O bonds, thereby facilitating bond activation and cleavage. [58] Consequently, the energy barriers for key elementary steps—particularly N–O bond dissociation and subsequent proton-coupled hydrogenation of *NO_x intermediates—are significantly reduced on the Co–Cu dual sites. Moreover, the alloyed interfacial environment provides moderated binding energies for critical reaction intermediates (*NO_2, *NO, and *NH_x), approaching the Sabatier optimum. This balance prevents both overly weak adsorption (typical of isolated Cu sites) and excessive overbinding (often observed on Co sites), leading to a lower limiting potential and more favorable reaction energetics. These results confirm that the enhanced catalytic performance of the CoCu sites originates from intrinsic synergy and interfacial dual-metal effects rather than from isolated single-metal adsorption. Based on these insights, two DFT-optimized reaction pathways (Pathway-1 and Pathway-2) for eNO_2RR on CuCoPBA/Cu_2S/Co_9S_8 were identified and are schematically illustrated in Fig. 7a. The Gibbs free-energy profiles indicate that the pathway *NO → *NH_2O →*NH_2OH→*NH_2→*NH_3 (Pathway-1) is energetically more favorable than the alternative *NO→*N→*NH→*NH_2→*NH_3 route (Pathway-2). The adsorption configurations of

View Article Online
DOI: 10.1039/D6IM00053C

reaction intermediates at the Cu site of Cu_2S and the Co site of Co_9S_8 at the CuCoPBA/Cu_2S/Co_9S_8 interface leading to NH_3 formation are shown in Fig. 7b. The calculated Gibbs-free energy profiles for the Co-site of CuCoPBA in CuCoPBA-S, the Cu-site of CuCoPBA in CuCoPBA-S, the Cu-site of Cu_2S, and the Co-site of Co_9S_8 are depicted in Fig. S40. Similarly, the calculated Gibbs-free energy profiles for the Co-site of CuCoPBA in CuCoPBA-S, the Cu-site of CuCoPBA in CuCoPBA-S, the Cu-site of Cu_2S in CuCoPBA-S, and the Co-site of Co_9S_8 in CuCoPBA-S are depicted in Fig. S41. In both cases, the potential determining step (PDS) is the hydrogenation of $*NH_2O$ to $*NH_2OH$. Among all Gibbs-free energy diagrams, the Co-site of CuCoPBA in CuCoPBA-S requires less energy for hydrogenation and subsequent electrochemical reduction to NH_3, highlighting its superior electrocatalytic activity for converting NO_2^- to NH_3 compared with the other sites.

View Article Online
DOI: 10.1039/D6IM00053C

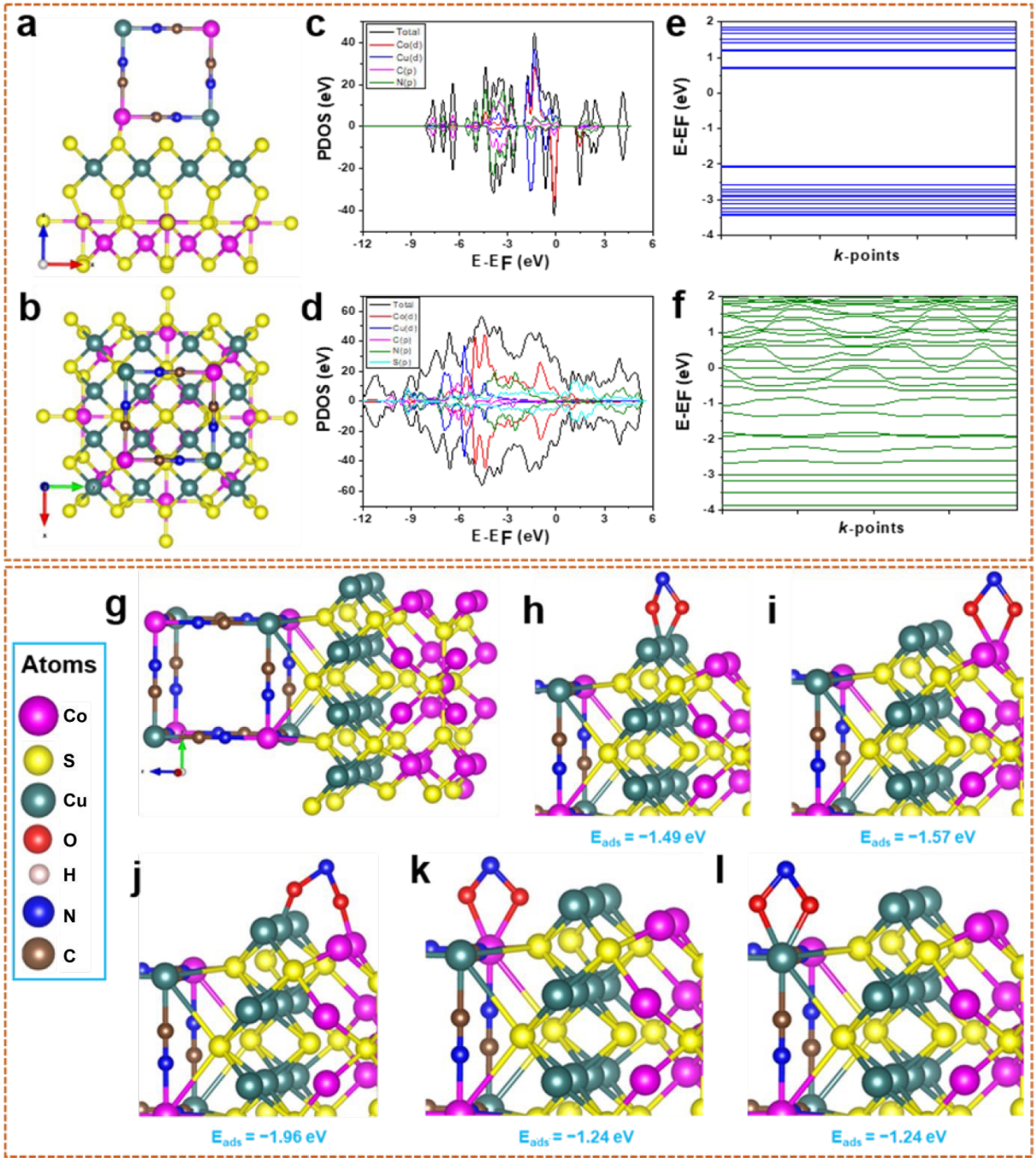

Fig. 6 (a) Top-view and (b) side-view of the DFT-optimized geometry of CuCoPBA-S; partial density of states (PDOS) for (c) CuCoPBA and (d) CuCoPBA-S; Band structure for (e) CuCoPBA and (f) CuCoPBA-S; Schematic representation of NO_2^- adsorption at various sites of the CuCoPBA/Cu_2S/Co_9S_8: (g) DFT-optimized geometry of CuCoPBA/Cu_2S/Co_9S_8, (h) NO_2^- adsorption at Cu-site of Cu_2S at interface of CuCoPBA/Cu_2S/Co_9S_8, (i) NO_2^- adsorption at Co-site of Co_9S_8 at interface of CuCoPBA/Cu_2S/Co_9S_8, (j) NO_2^- adsorption at Cu-site of Cu_2S and

View Article Online
DOI: 10.1039/D6IM00053C

Co-Site of Co_9S_8 at interface of $CuCoPBA/Cu_2S/Co_9S_8$, (k) NO_2^- adsorption at Co-site of CuCoPBA at interface of $CuCoPBA/Cu_2S/Co_9S_8$, and (l) NO_2^- adsorption at Cu-site of CuCoPBA at interface of $CuCoPBA/Cu_2S/Co_9S_8$.

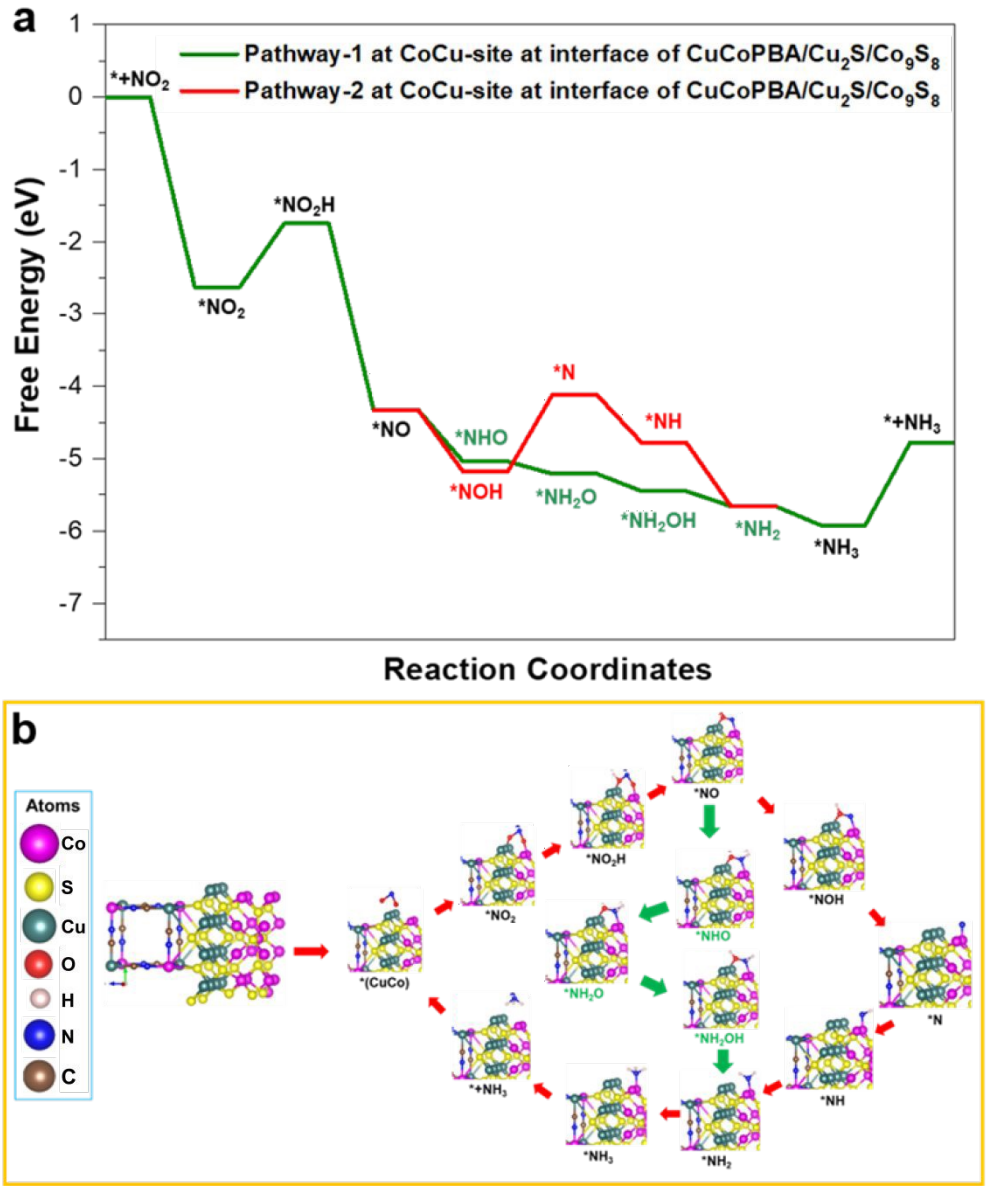

Fig. 7 (a) Gibbs free energy diagram for the two DFT-optimized reaction pathways during the eNO_2RR and (b) Schematic representation of the reduction of NO_2^- to NH_3^+ with various reaction pathways (Green Arrow: Pathway-1; Red Arrow: Pathway-2) over the surface of CuCoPBA-S interface.

View Article Online
DOI: 10.1039/D6IM00053C

3 Conclusions

In this study, we successfully synthesized CuCoPBA-S with a well-defined flower-like morphology via a facile PLIL strategy using CuCoPBA as the precursor. The formation mechanism of CuCoPBA-S was investigated via acoustic levitation coupled with PLIL method. The contaminant-free synthesis of CuCoPBA-S via acoustic levitation coupled with PLIL showed that the sulfidation process is time dependent, leading to the evolution of an ordered/disordered flower-like CuCoPBA-S heterostructure. Detailed FESEM and HRTEM analyses confirmed the preservation of the hierarchical flower-like architecture after laser processing. The as-synthesized CuCoPBA-S was then used as a catalyst for the electroreduction of NO_2^- to NH_3 via eNO_2RR. The CuCoPBA-S exhibited excellent catalytic activity toward the electroreduction of NO_2^- to NH_3, achieving a maximum FE (NH_3) of 80.91% and an YR (NH_3) of 3394.1 μg h^{-1} cm^{-2} at −0.5 V vs. RHE. Moreover, the catalyst demonstrated excellent operational stability, maintaining consistent electrochemical performance over 10 h of continuous eNO_2RR electrolysis at −0.5 V vs. RHE with hourly catholyte replacement. Post-reaction characterizations using XRD, FESEM, and SEM-EDX confirmed that the bulk structure and morphology of CuCoPBA-S were well preserved after prolonged operation. Mechanistic insights obtained from *in situ* Raman spectroscopy revealed the formation of key reaction intermediates including *NO, *NO_2, *NH_2, and *NH_2OH during the eNO_2RR pathway, which were further corroborated by *ex situ* FTIR analysis. DFT calculations demonstrated that NO_2^- adsorption at the Cu site of Cu_2S and the Co site of Co_9S_8 at the CuCoPBA/Cu_2S/Co_9S_8 interface is energetically most favorable for initiating eNO_2RR. In particular, bidentate NO_2^- adsorption across interfacial Co–Cu dual sites is thermodynamically superior to monodentate adsorption on isolated Cu or Co sites, owing to enhanced electronic coupling, stronger stabilization of intermediates, and more favorable reaction energetics. This

View Article Online
DOI: 10.1039/D6IM00053C

dual-site synergy significantly accelerates NO_2^- activation and improves both the kinetics and selectivity of NH_3 formation. Overall, this study introduces a novel strategy for elucidating the formation mechanisms of PLIL-derived catalysts by integrating *in situ* Raman spectroscopy with acoustic levitation.

4 Experimental section

4.1 Materials

Potassium hexacyanocobaltate(III) ($K_3[Co(CN)_6]$), copper nitrate ($Cu(NO_3)_2$), and sodium citrate ($Na_3C_6H_5O_7$) were purchased from Sigma-Aldrich. Deionized water was used in all experiments.

4.2 Synthesis of CuCoPBA and CuCoPBA-S

Initially, CuCoPBA nanocubes were synthesized via a modified coprecipitation method reported in the literature. [59] In a typical procedure, 2 mM $K_3[Co(CN)_6]$, 2 mM $Cu(NO_3)_2$, and 2.25 mM $Na_3C_6H_5O_7$ were dissolved in 20 mL of deionized water under magnetic stirring and let undisturbed for 24 h at room temperature. The resulting precipitate was collected via centrifugation at 8000 rpm for 5 min, washed several times with water, and dried in a vacuum oven at 60 ℃ for 6 h to obtain CuCoPBA powder. The as-prepared CuCoPBA was then used to synthesize CuCoPBA-S via acoustic levitation coupled with the PLIL method. In a typical procedure, 5 mg of CuCoPBA was dispersed in 10 mL of deionized water in a 20 mL glass vial, followed by the addition of 5 mg of thiourea and thorough stirring. The dispersion was then irradiated with a Ng:YAG laser (10 Hz, 7 ns) at 532 nm with a laser power of 200 mJ/pulse for 30 min. The resulting powder was filtered and dried at 60 ℃ to obtain CuCoPBA-S.

View Article Online
DOI: 10.1039/D6IM00053C

Details of material characterization, electrochemical measurements, NH_3 quantification using the calorimetric indophenol blue method and ^1H nuclear magnetic resonance (NMR), calculation of NH_3 yield rate (YR (NH_3)) and NH_3 Faradaic efficiency (FE (NH_3)), N_2 and H_2 quantification by gas chromatography (GC) method, H_2 yield rate (YR (H_2)) and H_2 Faradaic efficiency (FE (H_2)), *in situ* Raman spectroscopy measurements, acoustic levitation measurements, and DFT computations are provided in the Supporting Information.

Data availability

The data that support the findings of this study are available from the corresponding author upon reasonable request.

Author contributions

Juhyeon Park: conceptualization, data curation, investigation, writing – original manuscript. Jayesh Cherusseri: methodology, investigation, formal analysis, writing – review & editing. Jayaraman Theerthagiri: methodology, investigation, formal analysis, writing – review & editing. Ahreum Min: investigation, resources, writing – review & editing. Anuj Kumar: investigation, resources, writing – review & editing. Gyeong-Ah Kim: formal analysis, investigation. Nivarthi Rajiv Bharadwaj: Data curation, formal analysis, Sanggyeong Lee: investigation, formal analysis, Rimal Isaac R.S.: investigation, formal analysis. Myong Yong Choi: funding acquisition, project administration, resources, supervision, writing – review & editing.

View Article Online
DOI: 10.1039/D6IM00053C

Conflicts of interest

The authors declare no conflict of interest.

Acknowledgments

This research was supported by Korea Basic Science Institute (National research Facilities and Equipment Center) grant funded by the Ministry of Education (No. 2019R1A6C1010042, RS-2024-00434932, RS-2025-12872968, and 2021R1A6C102A526), and by the Korea government (MSIT) (PG2025039-02). The authors acknowledge financial support from National Research Foundation of Korea (NRF) (RS-2025-02634080, 2022R1A2C2010686, RS-2024-00405324, and RS-2024-00443792). This work was supported by the Research Resurgence under the Glocal University 30 Project at Gyeongsang National University in 2025.

References

1. J. Lim, C.-Y. Liu, J. Park, Y.-H. Liu, T. P. Senftle, S. W. Lee and M. C. Hatzell, Structure sensitivity of Pd facets for enhanced electrochemical nitrate reduction to ammonia, *ACS Catal.*, 2021, **11**, 7568-7577.
2. A. Castillo, K. Rigby, J.-H. Kim, J. L. Gardea-Torresdey and D. Villagrán, Selective nitrate reduction to ammonia at environmentally relevant concentrations with an iron-phthalocyanine polymer, *ACS Catal.*, 2024, **14**, 15489-15497.
3. S. Guo, K. Heck, S. Kasiraju, H. Qian, Z. Zhao, L. C. Grabow, J. T. Miller and M. S. Wong, Insights into nitrate reduction over indium-decorated palladium nanoparticle catalysts, *ACS Catal.*, 2018, **8**, 503-515.

View Article Online
DOI: 10.1039/D6IM00053C

4. H. Liu, J. Park, Y. Chen, Y. Qiu, Y. Cheng, K. Srivastava, S. Gu, B. H. Shanks, L. T. Roling and W. Li, Electrocatalytic nitrate reduction on oxide-derived silver with tunable selectivity to nitrite and ammonia, *ACS Catal.*, 2021, **11**, 8431-8442.

5. G. Qing, R. Ghazfar, S. T. Jackowski, F. Habibzadeh, M. M. Ashtiani, C.-P. Chen, M. R. Smith III and T. W. Hamann, Recent advances and challenges of electrocatalytic N_2 reduction to ammonia, *Chem. Rev.*, 2020, **120**, 5437-5516.

6. W. Go, R. A. Senthil, J. Cherusseri, A. Kumar, C. J. Moon, W. Limphirat, M. Ubaidullah and M. Y. Choi, Harnessing surface-tuned Ag/Cu interfaces in $Ag/Ag_2O/CuO$ for high-efficiency ammonia synthesis and Co-electricity generation in Zn–nitrate batteries, *Adv. Funct. Mater.*, 2025, **35**, e11876.

7. J. Kim, J. Cherusseri, J. Theerthagiri, A. Kumar and M. Y. Choi, Normal↔ inverse spinel nanocage charge modulation in nickel ferrite/nitrogen–doped carbon composite for efficient ammonia electrosynthesis and energy supply, *Chem. Eng. J.*, 2025, **525**, 170119.

8. A. R. Singh, B. A. Rohr, M. J. Statt, J. A. Schwalbe, M. Cargnello and J. K. Nørskov, Strategies toward selective electrochemical ammonia synthesis, *ACS Catal.*, 2019, **9**, 8316-8324.

9. R. Zhao, Q. Yan, L. Lu, L. Yu, H. Chen, T. Yan, L. Liu and J. Xi, Nitrite-mediated pulsed electrocatalytic nitrate reduction to ammonia over Co@Cu NW with dual active sites, *ACS Catal.*, 2024, **14**, 17046-17054.

10. Y. Wan, Y. Zhang, N. Zhang, Z. Zhang and K. Chu, Single-atom Zn on MnO_2 for selective nitrite electrolysis to ammonia, *Chem. Eng. J.*, 2024, **481**, 148734.

11. F. Wang, H. Zhao, G. Zhang, H. Zhang, X. Han and K. Chu, Electroreduction of nitrite to ammonia over Ni_1Ru single-atom alloys, *Adv. Funct. Mater.*, 2024, **34**, 2308072.

View Article Online
DOI: 10.1039/D6IM00053C

12. Y. Lee, J. Theerthagiri, N. Yodsin, A. Min, C. J. Moon, S. Jungsuttiwong and M. Y. Choi, Mitigating intraphase catalytic-domain transfer via CO_2 laser for enhanced nitrate-to-ammonia electroconversion and Zn-nitrate battery behavior, *Angew. Chem., Int. Ed.*, 2024, **136**, e202413774.

13. Q. Wang, X. Zhao, J. Zhang and X. Zhang, Investigation of nitrate reduction on polycrystalline Pt nanoparticles with controlled crystal plane, *J. Electroanal. Chem.*, 2015, **755**, 210-214.

14. Y. Zhang, X. Chen, W. Wang, L. Yin and J. C. Crittenden, Electrocatalytic nitrate reduction to ammonia on defective Au1Cu (111) single-atom alloys, *Appl. Catal. B*, 2022, **310**, 121346.

15. J. Liu, T. Cheng, L. Jiang, A. Kong and Y. Shan, Efficient nitrate reduction over novel covalent Ag-salophen polymer-derived "vein-leaf-apple"-like Ag@carbon structures, *ACS Appl. Mater. Interfaces*, 2020, **12**, 33186-33195.

16. Y. Yao, L. Zhao, J. Dai, J. Wang, C. Fang, G. Zhan, Q. Zheng, W. Hou and L. Zhang, Single atom Ru monolithic electrode for efficient chlorine evolution and nitrate reduction, *Angew. Chem., Int. Ed.*, 2022, **61**, e202208215.

17. J.-Y. Zhu, Q. Xue, Y.-Y. Xue, Y. Ding, F.-M. Li, P. Jin, P. Chen and Y. Chen, Iridium nanotubes as bifunctional electrocatalysts for oxygen evolution and nitrate reduction reactions, *ACS Appl. Mater. Interfaces*, 2020, **12**, 14064-14070.

18. Y. Guo, J. R. Stroka, B. Kandemir, C. E. Dickerson and K. L. Bren, Cobalt metallopeptide electrocatalyst for the selective reduction of nitrite to ammonium, *J. Am. Chem. Soc.*, 2018, **140**, 16888-16892.

View Article Online
DOI: 10.1039/D6IM00053C

19. V. Rosca, M. Duca, M. T. de Groot and M. T. Koper, Nitrogen cycle electrocatalysis, *Chem. Rev.*, 2009, **109**, 2209-2244.

20. Y. Wan, W. Du, K. Chen, N. Zhang and K. Chu, Electrocatalytic nitrite-to-ammonia reduction on isolated Cu sites, *J. Colloid Interface Sci.*, 2023, **652**, 2180-2185.

21. F. Wang, S. Shang, Z. Sun, X. Yang and K. Chu, Electrocatalytic nitrite reduction to ammonia on In_1Cu single atom alloy, *Chem. Eng. J.*, 2024, **489**, 151410.

22. Q. Li, Y. Li, D. Liu, H. Cai, E. Han, Y. He and X. Yang, Electroreduction from nitrite to ammonia over cobalt sulfide nanorods on nickel, *ACS Appl. Nano Mater.*, 2024, **7**, 17829-17839.

23. S. Liu, L. Cui, S. Yin, H. Ren, Z. Wang, Y. Xu, X. Li, L. Wang and H. Wang, Heterointerface-triggered electronic structure reformation: Pd/CuO nano-olives motivate nitrite electroreduction to ammonia, *Appl. Catal. B*, 2022, **319**, 121876.

24. J. Wang, J. Liang, P. Liu, Z. Yan, L. Cui, L. Yue, L. Zhang, Y. Ren, T. Li and Y. Luo, Biomass Juncus derived carbon decorated with cobalt nanoparticles enables high-efficiency ammonia electrosynthesis by nitrite reduction, *J. Mater. Chem. A*, 2022, **10**, 2842-2848.

25. L. Ouyang, X. Fan, Z. Li, X. He, S. Sun, Z. Cai, Y. Luo, D. Zheng, B. Ying and J. Zhang, High-efficiency electroreduction of nitrite to ammonia on a $Cu@TiO_2$ nanobelt array, *Chem. Commun.*, 2023, **59**, 1625-1628.

26. J. Liang, B. Deng, Q. Liu, G. Wen, Q. Liu, T. Li, Y. Luo, A. A. Alshehri, K. A. Alzahrani and D. Ma, High-efficiency electrochemical nitrite reduction to ammonium using a Cu_3P nanowire array under ambient conditions, *Green Chem.*, 2021, **23**, 5487-5493.

View Article Online
DOI: 10.1039/D6IM00053C

27. L. Hu, D. Zhao, C. Liu, Y. Liang, D. Zheng, S. Sun, Q. Li, Q. Liu, Y. Luo and Y. Liao, Amorphous CoB nanoarray as a high-efficiency electrocatalyst for nitrite reduction to ammonia, *Inorg. Chem. Front.*, 2022, **9**, 6075-6079.

28. G. Wen, J. Liang, Q. Liu, T. Li, X. An, F. Zhang, A. A. Alshehri, K. A. Alzahrani, Y. Luo and Q. Kong, Ambient ammonia production via electrocatalytic nitrite reduction catalyzed by a CoP nanoarray, *Nano Res.*, 2022, **15**, 972-977.

29. X. Fang, L. Tan, H. Luo, F. Jiang and H. Chen, Efficient electrochemical reduction of nitrate by bimetallic Cu-Fe phosphide derived from Prussian blue analogue, *Colloids Surf. A*, 2023, **658**, 130678.

30. T. Begildayeva, J. Theerthagiri, W. Limphirat, A. Min, S. Kheawhom and M. Y. Choi, Deciphering indirect nitrite reduction to ammonia in high-entropy electrocatalysts using in situ raman and X-ray absorption spectroscopies, *Small*, 2024, **20**, 2400538.

31. J. Theerthagiri, J. Park, M. A. Kumari, A. Kumar, Y. Oh and M. Y. Choi, High-entropy switching with 3*d* metal crossover sites for zinc–nitrite battery and ammonia supply, *Appl. Catal. B*, 2025, **378**, 125620.

32. C. Xin, Y.-P. Wei, J.-q. Bai, J. Chen, S. Sun and C.-J. Mao, Synergistic integration of copper and cobalt-MOF for high-efficiency electrocatalytic nitrate reduction to ammonia, *J. Environ. Chem. Eng.*, 2025, **13**, 115182.

33. W. He, J. Zhang, S. Dieckhöfer, S. Varhade, A. C. Brix, A. Lielpetere, S. Seisel, J. R. Junqueira and W. Schuhmann, Splicing the active phases of copper/cobalt-based catalysts achieves high-rate tandem electroreduction of nitrate to ammonia, *Nat. Commun.*, 2022, **13**, 1129.

View Article Online
DOI: 10.1039/D6IM00053C

34. C. Xiao, Y. Guo, J. Sun, T. Guo, X. Jia, S. Guo, G. Wu, Y. Sun, Z. Yao and Y. Liu, Efficient electrocatalytic reduction of nitrate to ammonia at low concentration by copper-cobalt oxide nanowires with shell–core structure, *Nano Res.*, 2024, **17**, 5087-5094.

35. Y. Feng, J.-T. Ren, M.-L. Sun and Z.-Y. Yuan, Valorization systems based on electrocatalytic nitrate/nitrite conversion for energy supply and valuable product synthesis, *Chem. Sci.*, 2025, **16**, 1528-1559.

36. J. Wang, T. Feng, J. Chen, V. Ramalingam, Z. Li, D. M. Kabtamu, J.-H. He and X. Fang, Electrocatalytic nitrate/nitrite reduction to ammonia synthesis using metal nanocatalysts and bio-inspired metalloenzymes, *Nano Energy*, 2021, **86**, 106088.

37. Y. Wang, Y. Xiong, M. Sun, J. Zhou, F. Hao, Q. Zhang, C. Ye, X. Wang, Z. Xu and Q. Wa, Controlled synthesis of unconventional phase alloy nanobranches for highly selective electrocatalytic nitrite reduction to ammonia, *Angew. Chem., Int. Ed.*, 2024, **136**, e202402841.

38. T. Begildayeva, J. Theerthagiri, V. T. Nguyen, A. Min, H. Shin and M. Y. Choi, Pulsed laser-initiated dual-catalytic interfaces for directed electroreduction of nitrite to ammonia, *Small Struct.*, 2024, **5**, 2400187.

39. C. J. Moon, V. Maheskumar, A. Min, A. Kumar, S. Lee, R. A. Senthil, M. Ubaidullah and M. Y. Choi, Laser-regulated iridium-diffused nitrogen–carbon sites for enhanced hydrazine-assisted alkaline seawater splitting and zinc–hydrazine batteries, *Small*, 2025, **21**, 2408569.

40. C. E. Park, J. Theerthagiri, V. Maheskumar, A. Kumar, G. H. Jeong and M. Y. Choi, Cocktail effect of 4d/5d band twisted high-entropy alloys on carbon nanotube for hydrazine splitting, *Small*, 2025, **21**, 2410304.

View Article Online
DOI: 10.1039/D6IM00053C

41. Y. Lee, J. Theerthagiri, W. Limphirat, G. Periyasamy, G. H. Jeong, S. Kheawhom, Y. Tang and M. Y. Choi, Pulsed laser-patterned high-entropy single-atomic sites and alloy coordinated graphene oxide for pH-universal water electrolysis, *J. Mater. Chem. A*, 2025, **13**, 9073-9087.

42. S. Sarsenov, R. A. Senthil, A. Min, A. Kumar, C. J. Moon, J. Park and M. Y. Choi, Deciphering the electronic coupling dynamics of laser-induced Ru/Cu electrocatalyst for dual-side hydrogen production and formic acid co-synthesis via DFT analysis, *Small*, 2025, **21**, 2403999.

43. J. Park, B. K. Sahu, C. J. Moon, J. Theerthagiri, A. Min, S. Yun and M. Y. Choi, Probing hydrogen evolution on pulsed laser-crafted Pt-infused oxygen-deficient black TiO_2 in real-time using raman spectroscopy, *J. Phys. Chem. C*, 2024, **128**, 14897-14906.

44. Q. Shi, W. Di, D. Dong, L. W. Yap, L. Li, D. Zang and W. Cheng, A general approach to free-standing nanoassemblies via acoustic levitation self-assembly, *ACS Nano*, 2019, **13**, 5243-5250.

45. J. Park, J. Theerthagiri, A. Min, C. J. Moon and M. Y. Choi, Laser-synthesized Ru-anchored few-layer black phosphorus for superior hydrogen evolution: Role of acoustic levitation, *ACS Appl. Mater. Interfaces*, 2024, **16**, 11561-11574.

46. B. B. Dangi and D. J. Dickerson, Design and performance of an acoustic levitator system coupled with a tunable monochromatic light source and a raman spectrometer for in situ reaction monitoring, *ACS Omega*, 2021, **6**, 10447-10453.

47. J. Park, A. Min, S. S. Naik, C. J. Moon, J. Theerthagiri and M. Y. Choi, In-situ monitoring of thiazine molecular aggregation in various solvents via a free-standing acoustic levitator, *Ultrason. Sonochem.*, 2023, **100**, 106609.

View Article Online
DOI: 10.1039/D6IM00053C

48. J. Park, A. Min, J. Theerthagiri, M. Ashokkumar and M. Y. Choi, In situ studies on free-standing synthesis of nanocatalysts via acoustic levitation coupled with pulsed laser irradiation, *Ultrason. Sonochem.*, 2023, **94**, 106345.

49. C. Han, L. Sun, S. Han and B. Liu, Stabilizing hydrogen radicals in two-dimensional cobalt -copper mesoporous nanoplates for complete nitrate reduction electrocatalysis to ammonia, *Angew. Chem. Int. Ed.*, 2025, **64**, e202416910.

50. D. Han, C. Li and H. Chen, The assignment of Co-C bond stretching vibrational frequency of CH_3Co (DH) $_2H_2O$ in IR and Raman spectra, *Spectrosc. Lett.*, 1998, **31**, 1263-1277.

51. J. Xu, D. Su, W. Zhang, W. Bao and G. Wang, A nitrogen–sulfur co-doped porous graphene matrix as a sulfur immobilizer for high performance lithium–sulfur batteries, *J. Mater. Chem. A*, 2016, **4**, 17381-17393.

52. E. Paulechka and A. Kazakov, Efficient ab initio estimation of formation enthalpies for organic compounds: Extension to sulfur and critical evaluation of experimental data, *J. Phys. Chem. A*, 2021, **125**, 8116-8131.

53. B. Lindberg, l. K. Hamrin, G. Johansson, U. Gelius, A. Fahlman, C. Nordling and K. Siegbahn, Molecular spectroscopy by means of ESCA II. sulfur compounds. Correlation of electron binding energy with structure, *Phys. Scr.*, 1970, **1**, 286.

54. E. Kurmaev, V. Fedorenko, V. Galakhov, S. Bartkowski, S. Uhlenbrock, M. Neumann, P. Slater, C. Greaves and Y. Miyazaki, Analysis of oxyanion (BO_3^{3-}, CO_3^{2-}, SO_4^{2-}, PO_4^{3-}, SeO_4^{4-}) substitution in Y123 compounds studied by X-ray photoelectron spectroscopy, *J. Supercond.*, 1996, **9**, 97-100.

View Article Online
DOI: 10.1039/D6IM00053C

55. W. Gao, K. Xie, J. Xie, X. Wang, H. Zhang, S. Chen, H. Wang, Z. Li and C. Li, Alloying of Cu with Ru enabling the relay catalysis for reduction of nitrate to ammonia, *Adv. Mater.*, 2023, **35**, 2202952.

56. L. Bai, F. Franco, J. Timoshenko, C. Rettenmaier, F. Scholten, H. S. Jeon, A. Yoon, M. Rüscher, A. Herzog and F. T. Haase, Electrocatalytic nitrate and nitrite reduction toward ammonia using Cu_2O nanocubes: Active species and reaction mechanisms, *J. Am. Chem. Soc.*, 2024, **146**, 9665-9678.

57. J. Abdul Nasir, J. Guan, T. W. Keal, A. W. Desmoutier, Y. Lu, A. M. Beale, C. R. A. Catlow and A. A. Sokol, Influence of solvent on selective catalytic reduction of nitrogen oxides with ammonia over Cu-CHA zeolite, *J. Am. Chem. Soc.*, 2022, **145**, 247-259.

58. Y. Wang, T. Wang, Q. Gu and J. Shang, Adsorption removal of NO_2 under Low-temperature and low - concentration conditions: A review of adsorbents and adsorption mechanisms, *Adv. Mater.*, 2025, **37**, 2401623.

59. C. Gu, L. Yang, M. Wang, N. Zhou, L. He, Z. Zhang and M. Du, A bimetallic (Cu-Co) Prussian Blue analogue loaded with gold nanoparticles for impedimetric aptasensing of ochratoxin a, *Microchim. Acta*, 2019, **186**, 1-10.

View Article Online
DOI: 10.1039/D6IM00053C

Data Availability

The data that support the findings of this study are available from the corresponding author upon reasonable request.